Title

Electrochemical Control of Magnetism on the Breathing Kagome Network of $Li_xScMo_3O_8$

Journal

Chemistry of Materials, 35(13)

ISSN

0897-4756 1520-5002

Authors

Wyckoff, Kira E
Kautzsch, Linus
Kaufman, Jonas L
et al.

Publication Date

2023-06-29

DOI

10.1021/acs.chemmater.3c00202

Peer reviewed

Electrochemical Control of Magnetism on the Breathing Kagome Network of $Li_xScMo_3O_8$

Kira E. Wyckoff,[†] Linus Kautzsch,[†] Jonas L. Kaufman,[†] Brenden R. Ortiz,[‡] Anna Kallistova,[†] Ganesh Pokharel,[‡] Jue Liu,[¶] Keith M. Taddei,[¶] Kamila M. Wiaderek,[§] Saul H. Lapidus,[‖] Stephen D. Wilson,[⊥] Anton Van der Ven,[*,†] and Ram Seshadri[*,†]

†*Materials Department and Materials Research Laboratory*
University of California, Santa Barbara, California 93106, United States
‡*Materials Department and California Nanosystems Institute*
University of California, Santa Barbara, California 93106, United States
¶*Neutron Scattering Division, Oak Ridge National Laboratory*
Oak Ridge, Tennessee, 37831, United States
§*X-ray Science Division, Advanced Photon Source, Argonne National Laboratory, Lemont, Illinois, 60439, United States*
‖*Joint Center for Energy Storage Research and X-ray Science Division, Advanced Photon Source, Argonne National Laboratory, Lemont, Illinois, 60439, United States*
⊥*Materials Department*
University of California, Santa Barbara, California 93106, United States
#*Department of Chemistry and Biochemistry*
University of California, Santa Barbara, California 93106, United States

E-mail: avdv@ucsb.edu; seshadri@mrl.ucsb.edu

Abstract

Controlling properties within a given functional inorganic material structure type is often accomplished through tuning the electronic occupation, which is in turn dictated by the elemental composition determined at the time of material preparation. We employ electrochemical control of the lithium content, with associated electronic occupancy control, to vary the magnetic properties of a material where a kagome-derived network of Mo_3 triangles carry the spin. In this case, Li is electrochemically inserted into $LiScMo_3O_8$, a layered compound containing a breathing Mo kagome network. Up to two additional Li can be inserted into $LiScMo_3O_8$, transforming it into $Li_3ScMo_3O_8$. $Li_2ScMo_3O_8$ prepared by electrochemical lithiation is compared to the quantum spin liquid candidate compound $Li_2ScMo_3O_8$ prepared through high-temperature solid-state methods, that has a slightly different structural stacking sequence but a similar kagome-derived network. Magnetic measurements are supported by first-principles calculations, showing that electrons remain localized on the Mo clusters throughout the doping series. As x is varied in $Li_xScMo_3O_8$, the measurements and calculations reveal the evolution from a diamagnetic band insulator at $x = 1$ to a geometrically frustrated magnet at $x = 2$, back to a diamagnetic insulator at $x = 3$. These results indicate a likelihood of strong coupling between the degree of Li disorder and charge/magnetic ordering over the Mo_3 clusters.

Introduction

While superficially appearing to comprise disjoint domains of investigation, magnetic materials and materials for electrochemical energy storage share a mutual reliance on the interplay between crystal and electronic structure, and oxidation state. Furthermore, these are often centered around d-block metals. A powerful example of this symbiosis is demonstrated by $LiCoO_2$, which was originally studied for its magnetic properties,[1] before it emerged much later to become the iconic cathode material.[2] Magnetic studies have continued to inform on the nature of several oxide cathode and anode materials.

In particular, magnetic studies have greatly impacted our understanding of complex mechanisms in a host of different material systems by probing electron spin.[3] Detailed study of the electronic phase diagram of Li_xCoO_2[4], $Li_{1-x}Fe_xMn_{1-x}PO_4$[5], and $LiNi_{0.8}Mn_{0.1}Co_{0.1}O_2$[6] using magnetometry has illuminated the sensitive influence of Li content on the complex electronic property evolution in these materials. In some members of the Wadsley-Roth family of fast-charging anode materials, magnetic measurements have been instrumental in supporting a hypothesized insulator to metal transition during cycling.[7,8] Advances in *operando* magnetometry have additionally revealed important insights towards design strategies in Sn-based alloy anodes.[9] On the device side, magnetic sensing has been shown to be a highly sensitive and quantitative technique for ascertaining cell health.[10]

Here we describe an electrode system based on a compound that can display geometric magnetic frustration and is closely related to candidate quantum spin liquid compounds, where electrochemical lithium insertion dramatically impacts magnetic properties. Geometrically frustrated networks, where all magnetic exchange pathways cannot be satisfied simultaneously, often give rise to complex and unconventional magnetic ground states. Ising spins on a triangular lattice lead to a large number of degenerate ground states.[11] This degeneracy has proved to be a defining characteristic of frustrated magnets,[12] leading to a wide variety of behaviors such as quantum spin liquid states,[13] and possible super-

conductivity.[14,15] Kagome networks are the maximally frustrated structures in 2D, and can be found in a variety of crystal structures. Characterized by corner-sharing triangles, the kagome network can be comprised of a wide variety of transition metals, such as Cu,[16] Mo,[17] Sn,[18] and V[19].

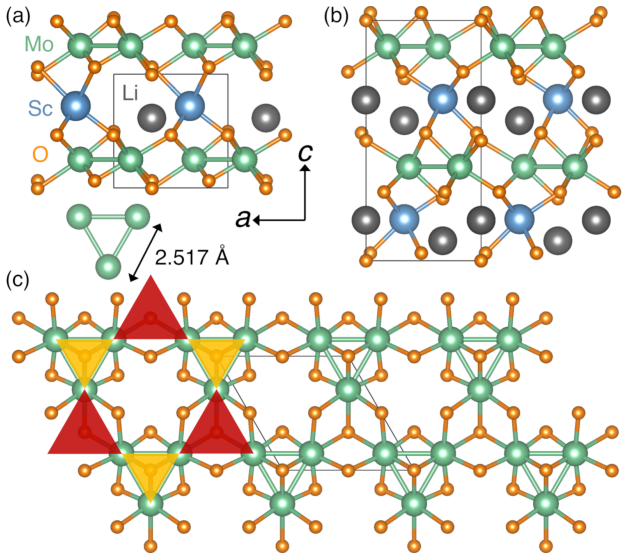

Figure 1: (a) Crystal structure of $LiScMo_3O_8$ (space group is $P3m1$, No. 156, O1 stacking) contains alternating layers of triangular clusters of metal-metal bonded Mo (green) atoms and Li^+ (grey)/Sc (blue). Li^+ is tetrahedrally coordinated. (b) Crystal structure of $Li_2ScMo_3O_8$ (h.t.) (space group is $P6_3mc$, No. 186, O2 stacking) contains slightly offset layers of triangular clusters of metal-metal bonded Mo atoms and Li^+/Sc. Li^+ is tetrahedrally coordinated.(c) Top view of two Mo-based breathing kagome-derived layers, indicated by the corner-connected smaller and larger triangles from $LiScMo_3O_8$, that is common to both structures.

Mott insulator phases in the $(A_nB_m)Mo_3O_8$, with two-dimensional slabs of a breathing Mo_3 kagome network, serve as a useful platform to study and understand quantum cluster magnets [Figure 1]. Kagome nets are defined by fully corner-connected equilateral triangles, and the term "breathing" here implies that alternate triangles are larger and smaller. The bonding scheme of these kagome networks allows for unpaired electrons to delocalize across clusters, as opposed to individual transition metals, and can serve as a structural platform to study exotic magnetism in extended solids. These Mo-based breathing kagome networks showcase notable diversity in magnetic behavior, even with seemingly minor

variations in composition and structure.[20,21] $LiZn_2Mo_3O_8$ is a cluster magnet that displays magnetic behavior[17] that is as-yet not well-understood. It has been postulated that the magnetic behavior may show features of a resonating valence-bond state,[22,23] dimerization,[24], or plaquette charge order.[25,26]

Recently, we showed that the breathing kagome-network compound $LiScMo_3O_8$, [Figure 1(a)] a diamagnetic insulator because of complete localization of two d electrons *per* Mo within Mo–Mo bonds, is an effective anode material for Li-ion batteries.[27] The related compound $Li_2ScMo_3O_8$, [Figure 1(b)] with an extra d electron for every 3 Mo also possesses a Mo-based breathing kagome network, shown in Figure 1(c), and is reported to be a frustrated cluster magnet,[28] with little sign of long range magnetic order down to $T = 0.5$ K. $Li_2In_{1-x}Sc_xMo_3O_8$ in contrast, where Sc is replaced by the smaller, isoelectronic In, has been noted to show antiferromagnetic long-range order through muon spin rotation experiments.[29]

Here, we have prepared the series of samples $Li_xScMo_3O_8$ in $x = 1.0$ to 2.85 by electrochemical insertion, and studied the evolution of magnetic properties *ex-situ*, across the series. Low temperature data show unusual behavior in electrochemically lithiated $Li_2ScMo_3O_8$ (e.c.) compared to high temperature $Li_2ScMo_3O_8$ (h.t.) phase, which has a distinctly different structure. Notably, the layer stacking in $Li_2ScMo_3O_8$ (e.c.) is O1 like the parent compound $LiScMo_3O_8$ [Figure 1(b)], while the layer stacking in $Li_2ScMo_3O_8$ (h.t.) is O2. In neither case is the Li expected to be stable in prismatic coordination.[30] Density function theory-based electronic structure calculations have been carried out that aid in the interpretation of the magnetic moment evolution. Through electrochemistry we can realize magnetic states that we otherwise would not be able to access through conventional synthetic routes, with the potential to lead to discovery of more applied functionality in the future.[31]

Methods

Preparation of $LiScMo_3O_8$ and $Li_2ScMo_3O_8$

Pristine $LiScMo_3O_8$ was prepared through a conventional high-temperature solid state reaction of precursor oxide powders in a sealed vitreous silica tube. Trace quantities of MoO_2 were removed with a dilute nitric acid wash to produce the pure target compound. A more detailed procedure can be found elsewhere.[27] $Li_2ScMo_3O_8$ was prepared in a similar manner using identical precursor oxide powders in the appropriate stoichiometry. For this composition, the nitric acid wash was not necessary. Both materials were black powders. Structural studies of the pristine compounds $LiScMo_3O_8$ and $Li_2ScMo_3O_8$ were carried out using neutron powder diffraction on the NOMAD beamline at Oak Ridge National Laboratory.

Electrochemical lithation of $LiScMo_3O_8$

A wide range of electrochemically lithiated samples were prepared using $LiScMo_3O_8$ as the starting material. Swagelok cells were used to prepare large quantities of lithiated material $Li_xScMo_3O_8$ in precise 0.25 Li increments. It is customary to prepare battery cells with additives such as binder and conductive carbons to improve transport and performance. For this study, all additives were omitted to maximize signal and avoid possible undesired magnetic contributions. Therefore, approximately 80 mg of pure starting $LiScMo_3O_8$ material was pressed in a 10 mm die to 4 tons to create a fragile, but thin and compact disk pellet. This pellet was delicately placed into a half assembled Swagelok cell. A glass fiber separator (Whatman GF/D) was gently placed on top of the pellet. This assembly was then pumped into an Ar-filled glovebox to complete the cell fabrication. Electrolyte (1 M $LiPF_6$ in ethylene carbonate/dimethyl carbonate (EC/DMC) 50/50 v/v Sigma Aldrich) was evenly dispersed on top of the separator. The quantity varied slightly, but enough electrolyte was used to just soak the separator. Polished Li foil was used as the counter

electrode and only light pressure was used to close the cell to avoid pellet disintegration. The cells were then discharged to insert Li at very slow rates, ranging from C/80 (80 hour discharge) to C/130 (130 hour discharge). The C rate was determined assuming 2 Li insert into the structure. Cells were discharged using a VMP3 BioLogic potentiostat. Each electrochemically lithiated composition was prepared in a different Swagelok cell.

Samples for the low temperature neutron study on the WAND^2 beamline at ORNL were prepared in a very similar manner. There were two main differences. Importantly, the sample size was increased from approximately 80 mg in small Swagelok cells to upwards of 300 mg using larger custom Swagelok cells. The custom larger Swagelok cell design is identical to the smaller Swagelok, except for the body diameter. The smaller typical Swagelok cells have a diameter of 13 mm and the larger Swagelok cells used in this study have a diameter of 20 mm. The pellet preparation is identical for both cells in terms of diameter and mass of the pellet. The advantage for the larger cell comes because only one 80 mg pellet can fit in the normal Swagelok while it is possible to fit approximately three of those same pellets in the large Swagelok. With this design, we can retain similar experimental parameters, but get larger yields of *ex-situ* powder. Second, instead of natural Li as the counter electrode, isotopically enriched ^{7}Li was used to increase scattering quality. An overlay of representative discharge curves can be found in the Supporting Information (SI).

Following completion of electrochemical Li insertion, the cells were then pumped back into an Ar-filled glovebox and kept strictly air-free for preparation, storage, and all characterization techniques to avoid any possible sample decomposition. The cells were carefully taken apart and the lithiated pellets were removed and left to dry overnight. Then they were crushed and lightly ground, moved into a centrifuge tube, and washed in EC:DMC to remove any residual surface salts. The effluent was poured off and the powders were vacuum dried for 2 hr to 3 hr, followed by gentle grinding in an agate mortar and pestle, resulting in a fine, black powder. These electrochemically lithiated powders were the basis

of all future measurements.

Diffraction data collection and reduction

Structural studies of the pristine compounds $LiScMo_3O_8$ and $Li_2ScMo_3O_8$ were carried out by collecting neutron total scattering data on the NOMAD beamline at Oak Ridge National Laboratory. For the current experiment, about 100 mg powder samples were loaded into 3 mm thin-walled quartz capillaries.[32,33] Two 24 min scans (at 290 K) were collected for each sample and then summed together to improve the statistics of the data. Scattering signal from the empty quartz capillaries measurements was subtracted as background from the sample measurement and data were normalized by the scattering intensity from a 6 mm vanadium rod to account for incident spectrum profile and detector efficiencies.

Rietveld refinements to the previously published structures[34] were carried out in the TOPAS v6 software.[35] Time-of-flight (TOF) data were converted to d-spacing data using the conventional second order polynomial TOF = ZERO + DIFC$\times d$ + DIFA$\times d^2$, where the parameters ZERO and DIFC were determined from refinement of a standard NIST Si-640e data set and held fixed, while the parameter DIFA was allowed to vary during refinements to account for sample displacement. A back-to-back exponential function convoluted with a Pseudo-Voigt function was used to describe the peak profile.[36] Lorentz factor is corrected by multiplying d^4.[37]

Structural studies of the lithiated $Li_2ScMo_3O_8$ (e.c) material were carried out on the WAND^2 HB-2C beamline at HFIR at Oak Ridge National Laboratory. Electrochemically lithiated powder at this composition was pressed into a 6 mm pellet and placed in a sealed vanadium can inside of a glovebox. The sample was measured in field-cooled warming conditions at a field of $H = 3$ T at temperatures ranging from $T = 2$ K to $T = 30$ K. Measurement time at each condition was correlated to the number of counts to ensure comparable data sets. Order parameters were calculated by integrating the intensity of each peak at every measured temperature.

Operando powder diffraction measurements were carried out at beamline 11-BM at the Advanced Photon Source at Argonne National Laboratory. All measurements were performed in an AMPIX cell[38] at room temperature in transmission geometry at wavelength ($\lambda = 0.458924$ Å). Pressed pellet electrodes were made in a 6:2:2 (active: SuperP: PTFE) mass ratio. The electrode weighed 21.1 mg and was 10 mm in diameter. The AMPIX cell was assembled in an argon glovebox using lithium metal as the counter electrode, a glass fiber seperator (Whatman), and 1.0 M $LiPF_6$ dissolved in 1:1 v/v ethylene carbonate/diethyl carbonate (EC/DEC). The cell was cycled at a C/15 rate. The diffraction patterns for $Li_2ScMo_3O_8$ (e.c.) and $Li_3ScMo_3O_8$ (e.c.) were extracted from this data set and background subtracted from a blank AMPIX cell. Rietveld refinements were performed using the calculated $Li_2ScMo_3O_8$ (e.c.) and $Li_3ScMo_3O_8$ (e.c.) ground state structures. All visualization involving crystal structures was carried out using VESTA.[39]

Characterization

Magnetic measurements were carried out on a Quantum Design MPMS3 SQUID magnetometer. Powder masses of approximately 5 mg were measured in polypropylene capsules. All samples were packed in an Ar-filled glovebox and kept in a vacuumed transfer container until just prior to MPMS loading. DC susceptibility measurements were collected in both field-cooled warming (FCW) and zero-field-cooled warming (ZFCW) conditions with applied magnetic fields H ranging from $H = 0.01$ T to $H = 5$ T in the temperature range $T = 2$ K to $T = 400$ K. Heat capacity measurements were carried out on a Quantum Design PPMS. The electrochemically lithiated powder was pressed inside of an Ar-filled glovebox to form a small pellet. This pellet was kept in a vacuumed transfer container until just before loading onto the heat capacity puck outside of the glovebox. The material was exposed to air for less than 1 min before PPMS measurement. Sintered pellets of $LiScMo_3O_8$ and $Li_2ScMo_3O_8$ (h.t.) were used to measure electrical resistivity in a Quantum Design PPMS. Gold wires were attached to the samples using silver paint to perform a four-point

measurement.

Computational Methodology

Electronic structure calculations using density functional theory (DFT) were performed with the Vienna *ab initio* Simulation Package (VASP).[40–43] The Li sv, Sc sv, Mo sv, and O projector augmented wave (PAW) pseudopotentials[44,45] were used with a plane-wave energy cutoff of 650 eV. Γ-centered Monkhorst-Pack k-meshes[46] were automatically generated with a density of 40 Å and integrated using the linear tetrahedron method.[47] The SCAN meta-GGA functional[48,49] was employed to approximate the exchange-correlation energy.

Results and discussion

Electronic structure

The crystal structure of $LiScMo_3O_8$ serves as the model platform for this study. $LiScMo_3O_8$ is a layered structure, with alternating layers of Mo and Li/Sc, as shown in Figure 1(a). The Mo layer is comprised of a Mo kagome network, built of metal-metal bonded MoO_3 clusters. In the alternating layer, Sc is octahedrally coordinated and Li is tetrahedrally coordinated. Bond valence sum mapping has shown that the Li/Sc layer has channels that allow for low-energy two dimensional Li diffusion pathways. It has also been shown recently that Li insertion into the structure is highly stable and reversible, with minimal changes or expansion of the network.[27] The starting oxidation state of Mo in this structure is Mo^{4+}, and previous electrochemistry of the compound shows that up to two additional Li can be inserted to achieve a total Li content of $Li_3ScMo_3O_8$. The parent structure is very similar to the more studied $Li_2ScMo_3O_8$ (h.t.) in Figure 1(b). $Li_2ScMo_3O_8$ is an established quantum spin liquid candidate with one unpaired e^- per Mo_3 cluster.[21,28,29,50] Compared to

$LiScMo_3O_8$, the Mo layers in this structure are slightly offset from each other and the Li occupy both sublattices of tetrahedral sites, rather than just one. The Mo layer of $LiScMo_3O_8$ is shown in Figure 1(c) with oxygen connectivity.

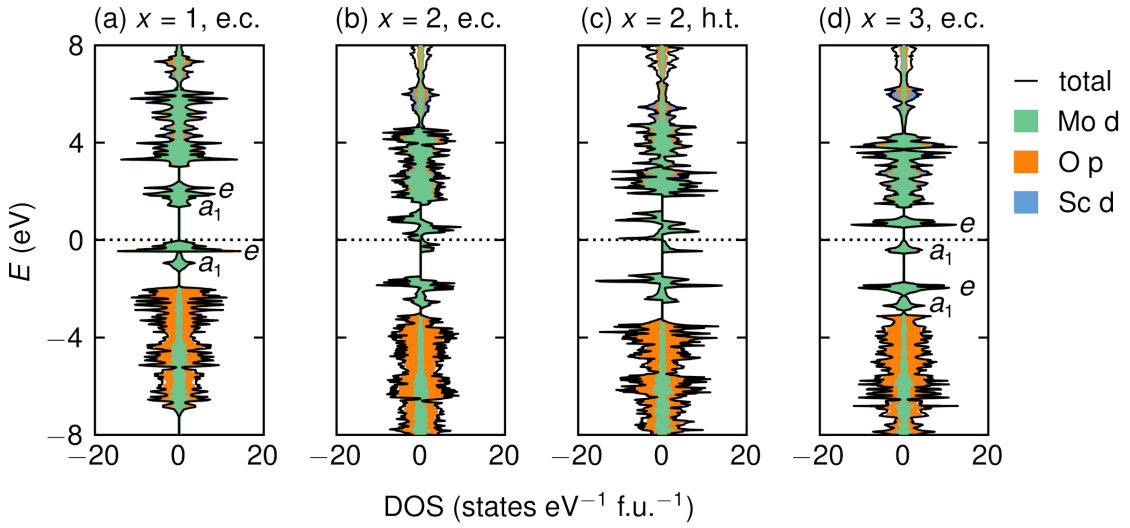

Figure 2: Spin-polarized density of states of $Li_xScMo_3O_8$ in either the electrochemical or high temperature structure at (a) $x = 1$, (b,c) $x = 2$, and (d) $x = 3$.

To better understand the relationship between the crystal structure and electronic structure of $Li_xScMo_3O_8$, DFT-based electronic structure calculations are used to provide qualitative insight about this material at different Li, or doping, levels. The density of states for pristine $LiScMo_3O_8$ is shown in Figure 2(a), annotated with the corresponding energy levels. The density of states shows filled Mo d-states just below the Fermi level, a large band gap, and no unpaired e^-, indicative of an insulator. If one additional Li is inserted into the structure, the nominal composition becomes $Li_2ScMo_3O_8$ and results in one unpaired e^- according to the energy level diagram displayed in Figure 3. The density of states for this composition is displayed in Figure 2(b) and shows that the spins become polarized. The states remain very localized, however, and the small dispersion indicates it is unlikely this material would be a good conductor.

Figure 2(c) shows the analogous density of states for the solid state preparation of $Li_2ScMo_3O_8$ (h.t.). Globally, the features in the density of states between $Li_2ScMo_3O_8$ (e.c.)

prepared electrochemically and $Li_2ScMo_3O_8$ (h.t.) prepared through solid state methods are close in semblance. If two additional Li are inserted into $LiScMo_3O_8$ to get a composition of $Li_3ScMo_3O_8$, the a_1 energy level fills and the electrons pair up. The density of states in Figure 2(d) shows that the gap between filled and unfilled states is much smaller than the pristine material, but a localized and insulating state is still expected. Electrical resistivity measurements (shown in the SI) on $LiScMo_3O_8$ and $Li_2ScMo_3O_8$ (h.t.) indeed show that $LiScMo_3O_8$ is orders of magnitude more resistive than $Li_2ScMo_3O_8$ (h.t.), and that $Li_2ScMo_3O_8$ (h.t.) displays not metallic, but semiconducting behavior. The electronic structure calculations and energy level diagram will be an important point of reference as we experimentally explore electrochemical doping of the $LiScMo_3O_8$ structure.

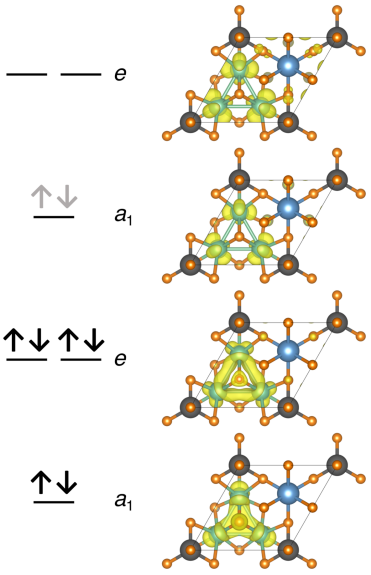

Figure 3: Left: Orbital energy level diagram for a single Mo_3 cluster, with black arrows showing the electron filling at $x = 1$ ($[Mo_3]^{12+}$) and gray arrows showing the additional electrons at $x = 3$ ($[Mo_3]^{10+}$). Right: Partial charge densities corresponding to the lower and upper a_1 and e states of a Mo_3 cluster in $LiScMo_3O_8$.

Figure 3 illustrates the partial charge densities corresponding to the lower and upper a_1 and e states of a Mo_3 cluster in $LiScMo_3O_8$. Parent material $LiScMo_3O_8$ begins with the lower a_1 and e states completely filled. The charge density for these states is localized on the Mo_3 cluster, distributed along their shared oxygen bonds and metal-metal bonds,

respectively. As Li and electrons are inserted and fill the upper a_1 state, the charge density localizes on the individual Mo atoms.

Diffraction and Electrochemistry

Both the starting material $LiScMo_3O_8$ and $Li_2ScMo_3O_8$ (h.t.) were characterized with neutron powder diffraction at the NOMAD beamline located at Oak Ridge National Laboratory. Rietveld refinements of both materials show good agreement with the accepted structures and can be found in the SI. An *operando* cycling experiment was performed at beamline 11-BM at Argonne National Laboratory to understand the structural evolution of the material $LiScMo_3O_8$ with lithium insertion and deinsertion. Figure 4 shows the electrochemisty and corresponding diffraction data over two complete galvanostatic cycles. As lithium is inserted, diffraction data indicate that the structure experiences minimal changes. The slight shifts and emergence of new peaks are both reversible and consistent with phase-coexistence regions. Although these features agree well with a previous *operando* lab powder x-ray diffraction experiment,[27] higher resolution synchrotron data allows for Rietveld refinements to the calculated ground state structures.

The black arrows in Figure 4 indicate the diffraction data that was extracted from the *operando* cycling experiment, corresponding to compositions $Li_2ScMo_3O_8$ (e.c.) and $Li_3ScMo_3O_8$ (e.c.). Figure 5 shows the Rietveld refinements for both materials using their respective ground state structures determined from ab-initio calculations. Refinement of $Li_2ScMo_3O_8$ (e.c.) is displayed in Figure 5 (a) and Figure 5 (b) shows the refinement of $Li_3ScMo_3O_8$ (e.c.), close to the maximum lithiation amount. Comparison of these individual diffraction traces more clearly highlights the emergence of additional diffraction peaks at low *Q*. Agreement between the experimental and calculated structures confirms the nuanced differences in the crystal structures at different lithiation levels.

The crystal structures of the thermally prepared compounds $LiScMo_3O_8$ and $Li_2ScMo_3O_8$ (h.t.) are shown in Figure 6 (a) and Figure 6 (b), respectively. The intralayer

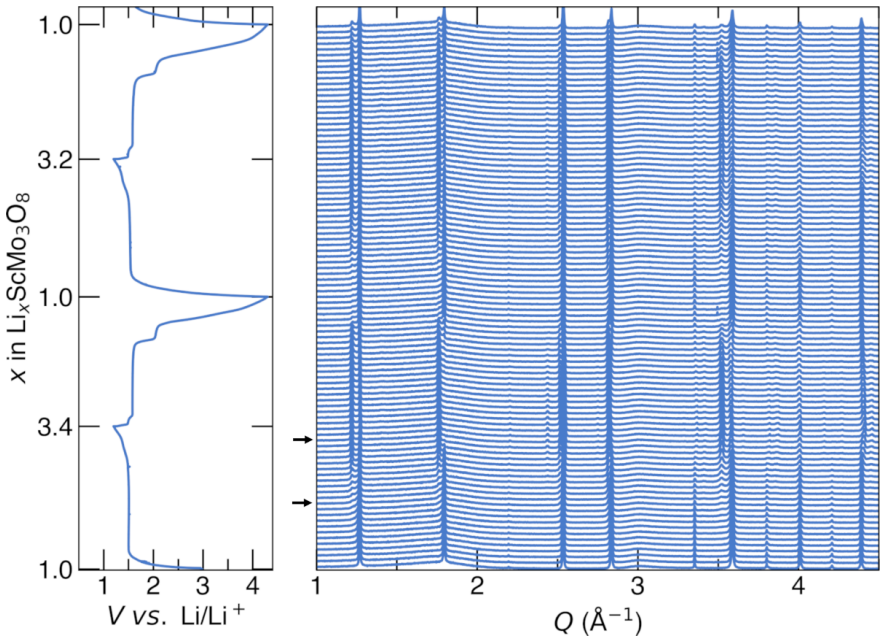

Figure 4: *Operando* synchrotron X-ray diffraction collected at 11-BM at APS of $LiScMo_3O_8$ during the first two galvanostatic discharge/charge cycles at a C/15 cycling rate. The electrochemistry is shown in the left panel. Arrows indicate the traces that were extracted from the data set and refined in Figure 5.

view of these structures again showcases the differences in layer stacking, with offset Mo layers in the $Li_2ScMo_3O_8$ (h.t.) material. Refined crystal structures of electrochemically prepared compounds $Li_2ScMo_3O_8$ (e.c.) [Figure 6 (c)] and $Li_3ScMo_3O_8$ (e.c.) [Figure 6 (d)] from the data shown in Figure 5 are shown below the thermally prepared compounds. While $Li_2ScMo_3O_8$ (h.t.) has offset Mo layers, $Li_2ScMo_3O_8$ (e.c.) and $Li_3ScMo_3O_8$ (e.c.) retain the same layer stacking as parent material $LiScMo_3O_8$.

Figure 7 shows an analogous comparison of the breathing kagome networks of these materials. Notably, the Mo layers in $LiScMo_3O_8$ [Figure 7 (a)] are aligned, while the offset Mo layers of $Li_2ScMo_3O_8$ (h.t.) [Figure 7 (b)] with O2 stacking is prominent. Electrochemically prepared $Li_2ScMo_3O_8$ [Figure 7 (c)] and $Li_3ScMo_3O_8$ (e.c.)[Figure 7 (d)] have very similar breathing kagome networks as the parent material. A "breathing ratio" can be calculated to better understand bond distances and connectivity in this type of kagome network, defined by the bond distance of the larger triangles divided by the bond distance of the smaller triangles, $\lambda = d_{\bigtriangledown}/d_{\bigtriangleup}$. The λ for the starting material $LiScMo_3O_8$ is 1.27

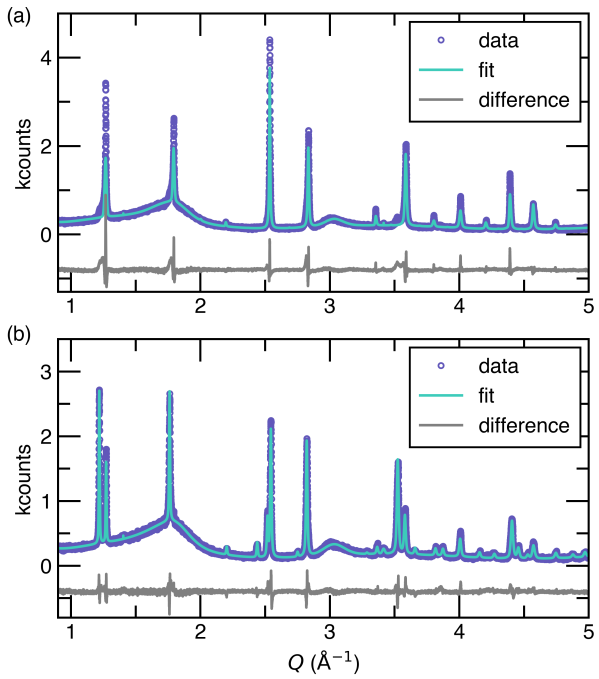

Figure 5: Rietveld refinements of (a) $Li_2ScMo_3O_8$ (e.c.) and (b) $Li_3ScMo_3O_8$ (e.c.) of *operando* synchrotron powder diffraction data collected at 11-BM at APS. These diffraction patterns were extracted from the *operando* AMPIX experiment and fit to the calculated ground state structures. The backgrounds were fit and only the lattice parameters and transition metal sites were allowed to refine. The refined crystallographic parameters can be found in the SI.

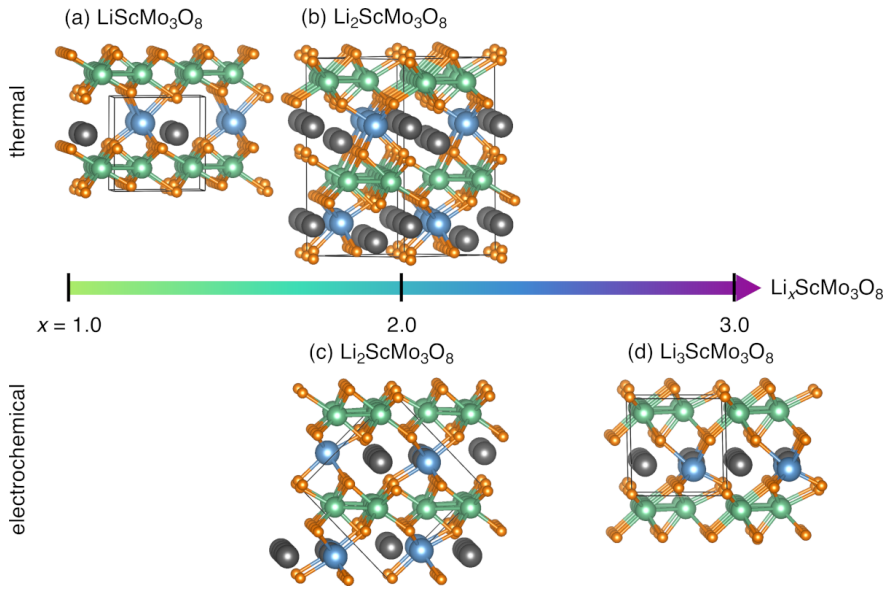

Figure 6: Diagram comparing the intralayer view of the discussed crystal structures. The top compounds (a) $LiScMo_3O_8$ and (b) $Li_2ScMo_3O_8$ (h.t.) are prepared through conventional high temperature methods and the compounds (c) $Li_2ScMo_3O_8$ (e.c.) and (d) $Li_3ScMo_3O_8$ (e.c.) are prepared electrochemically. $Li_2ScMo_3O_8$ (h.t.) shown in (b) has offset Mo layers with O2 stacking, while $LiScMo_3O_8$ in (a), and electrochemically prepared materials (c) $Li_2ScMo_3O_8$ (e.c.) and (d) $Li_3ScMo_3O_8$ (e.c.) have O1 stacking.

and the λ for $Li_2ScMo_3O_8$ (h.t.) is 1.28. From this standpoint, the kagome networks of these two materials are very similar and close to previous reports.[29] We find that electrochemical insertion of Li does not significantly alter λ. $Li_2ScMo_3O_8$ (e.c.) has a λ of 1.27, while $Li_3ScMo_3O_8$ (e.c.) has a λ of 1.24 . The slightly lower value of λ indicates that this material is closer to an ideal kagome network, where the bond lengths would all be equal. As Li is inserted, electrons begin to populate the antibonding a_1 states, as discussed in the next section.

Magnetic properties

It is possible to directly insert additional Li into $LiScMo_3O_8$ by using Li metal as the counter electrode while discharging a battery cell. Samples were prepared by electrochemically inserting Li into $LiScMo_3O_8$ in $x = 0.25$ increments. As opposed to more traditional coin cells that handle cast electrodes with a low material loading (up to 10 mg cm^{-2}), Swagelok cells

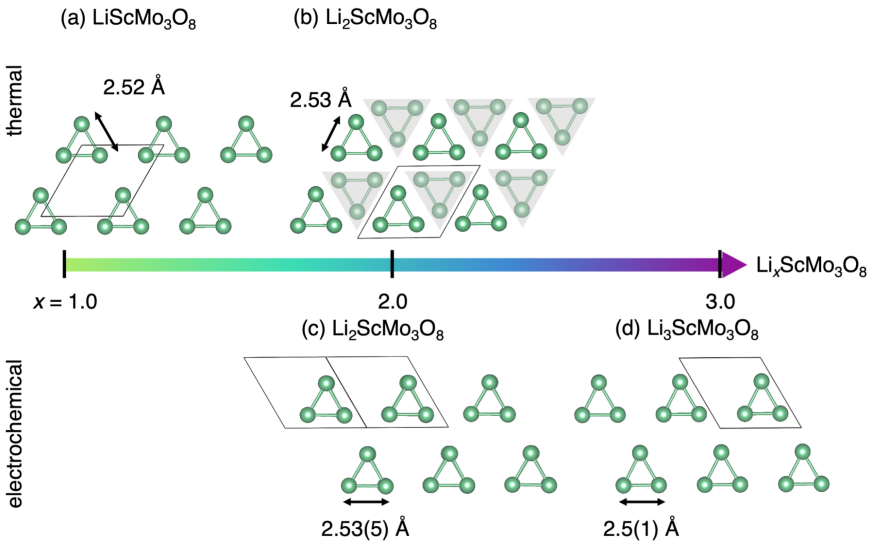

Figure 7: Diagram comparing the breathing kagome networks of the discussed crystal structures. Compounds (a) $LiScMo_3O_8$ and (b) $Li_2ScMo_3O_8$ (h.t.) are prepared through conventional high temperature methods and compounds (c) $Li_2ScMo_3O_8$ (e.c.) and (d) $Li_3ScMo_3O_8$ (e.c.) are prepared electrochemically. In (b), the two distinct layers of Mo_3 triangles are displayed with one of the layers being shaded. Average Mo–Mo bond distances are similar between the compounds.

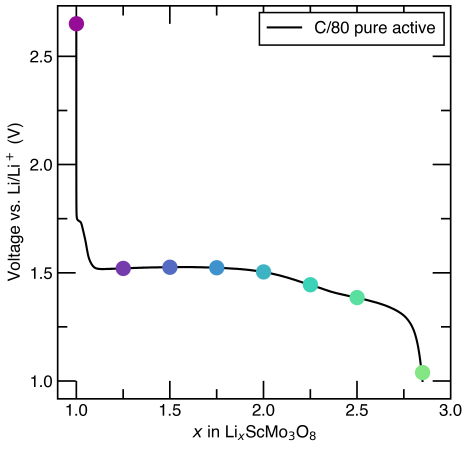

Figure 8: Electrochemical insertion of Li into $LiScMo_3O_8$ in a Swagelok cell. No binder or carbon was used for the electrochemistry. Each point on the discharge curve represents a single battery that was stopped in $x = 0.25$ increments. Galvanostatic cycling was performed at slow rates of C/80.

are amenable to much higher loading (up to 80 mg cm^{-2}) and can be disassembled in a glovebox to recover *ex-situ* material. The SI carries a depiction of an actual Swagelok cell, with a scheme of a typical internal battery stack. Galvanostatic cycling was used to apply a constant current until the specified Li content was reached. Figure 8 shows an actual discharge curve of pure active material at a slow cycling rate. Each point on the curve represents an individual battery cell and the shapes of all of the experimental voltage curves match the expected electrochemistry for this material, including the characteristic 1.5 V plateau.[27] The cells were brought back into the glovebox, disassembled, and prepared for subsequent characterization.

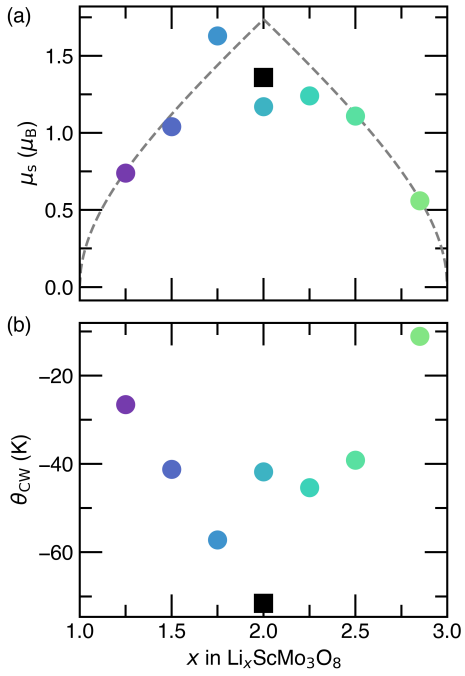

Figure 9: Summary of spin-only moment and Curie-Weiss temperatures extracted from Curie-Weiss fits as a function of x. Individual fits can be found in the SI. Colored points represent electrochemically lithiated $LiScMo_3O_8$ (e.c.) samples and the square black points represent the high temperature $Li_2ScMo_3O_8$ (h.t.) sample. (a) μ_s gives insight into the number of unpaired e^- in the system. μ_s increases until approximately $x = 2.0$ and then collapses back to original value. The grey dashed line represents the calculated spin only magnetic moment for one unpaired e^-. (b) Curie-Weiss temperature (θ_{CW}) as a function of x shows increasing AFM exchange strength towards $x = 2$, decreasing past this point.

Combining the results of the Curie-Weiss fits with the calculated charge densities pro-

vides a comprehensive picture of electron filling and localization for this Mo-based cluster magnet. SQUID magnetometry was used to measure the susceptibility of each electrochemically prepared sample at $H = 0.1\,\mathrm{T}$ between $T = 2\,\mathrm{K}$ and $T = 300\,\mathrm{K}$. An overlay of these susceptibility curves (shown in the SI) show clear evolution with varying Li content. At room temperature, the susceptibility is negative, consistent with diamagnetic behavior. As the Li content is increased, the susceptibility gradually increases until approximately $x = 2.0$. After this point, the susceptibility decreases, collapsing near the value of the original un-lithiated material. This is in qualitative agreement with the proposed energy level diagram.

Curie-Weiss fits to the susceptibility measurements can additionally provide more quantitative insight. Figure 9 summarizes the spin-only moments (μ_s) and Curie-Weiss temperatures (θ_{CW}) as a function of Li content. The trend visualized in the raw susceptibility data is reflected in the Curie-Weiss spin-only moments shown in Figure 9(a). As Li is inserted into $LiScMo_3O_8$, μ_s increases, maximizing around $x = 2.0$. Upon further lithiation, μ_s decreases back down. This trend fairly accurately tracks with the calculated spin only magnetic moment for one unpaired e^-. Experimental agreement with the calculated moment definitively confirms an electronic picture in which inserted electrons remain localized on the Mo_3 clusters. We note that the μ_s value of the $Li_2ScMo_3O_8$ (e.c.), a colored point, and $Li_2ScMo_3O_8$ (h.t.), a black square, are similar, indicating that the overall Li and electron counts for both compounds are very close.

Figure 9(b) shows that the Curie-Weiss temperatures also show a decisive trend. For the entire series, θ_{CW} is negative and decreases further with additional lithiation. The maxima in μ_s correlates to a minima in θ_{CW}, at values near $x = 2.0$. θ_{CW} becomes less negative past this point. Negative θ_{CW} values indicate that the exchange in this system is dominated by AFM interactions that get stronger as the number of unpaired e^- maximizes. Unlike the close agreement between the $Li_2ScMo_3O_8$ (e.c.) and $Li_2ScMo_3O_8$ (h.t.) samples for μ_s, there is a notable difference in θ_{CW}. This likely stems from key differences between

the two compounds relating to a combination of Li and charge ordering which will be discussed later.

Low-temperature magnetic properties

We observe notable low-temperature magnetic behavior in electrochemically lithiated $LiScMo_3O_8$. As demonstrated previously, we observe high-temperature behavior consistent with electron localization. However, at low temperatures, intermediate Li compositions ($x = 1.25-2.50$ in $Li_xScMo_3O_8$) all display a prominent feature at 12 K in susceptibility measurements, namely an abrupt change in slope. All of the temperature-dependent susceptibility traces, offset along the y-axis for clarity, are displayed in the SI. As more Li and electrons are introduced into the system, the slope change becomes steeper and the feature onset subtly increases until approximately $x = 2.0$. This suggests a possible correlation of the feature with both the maxima in μ_s and minima in θ_{CW}. Both the slope and onset temperature decrease until maximum lithiation at $x = 2.85$, when the upper a_1 state is nominally filled and the low-temperature feature disappears.

To gain more understanding related to the origin of this feature we compare electrochemically lithiated $Li_2ScMo_3O_8$ (e.c.) to high-temperature $Li_2ScMo_3O_8$ (h.t.). Figure 10(a) compares the low-temperature susceptibility of both compounds. $Li_2ScMo_3O_8$ (h.t.) shows no signs of long-range magnetic order to 2 K, consistent with literature on this quantum spin liquid candidate.[28] Conversely, $Li_2ScMo_3O_8$ (e.c.) displays a sharp slope change at 12 K. To confirm that the feature is a bulk property, heat capacity measurements in Figure 10(b) show a relatively broad peak that begins at the same temperature as the slope change in susceptibility. The heat capacity of the parent material $LiScMo_3O_8$ is smooth down to 2 K. The heat capacity data of $Li_2ScMo_3O_8$ (e.c.) were fit to a double-Debye function from 120 K and extrapolated down to 0 K from the equation in Fortes et al.[51] The peak feature was excluded from the range. The parameters resulting from the fit of this function to C_p are; $\theta_D^A = 717$ K, $\theta_D^B = 227$ K, $X = 0.89$, and $Y = 0.09$. The magnetic

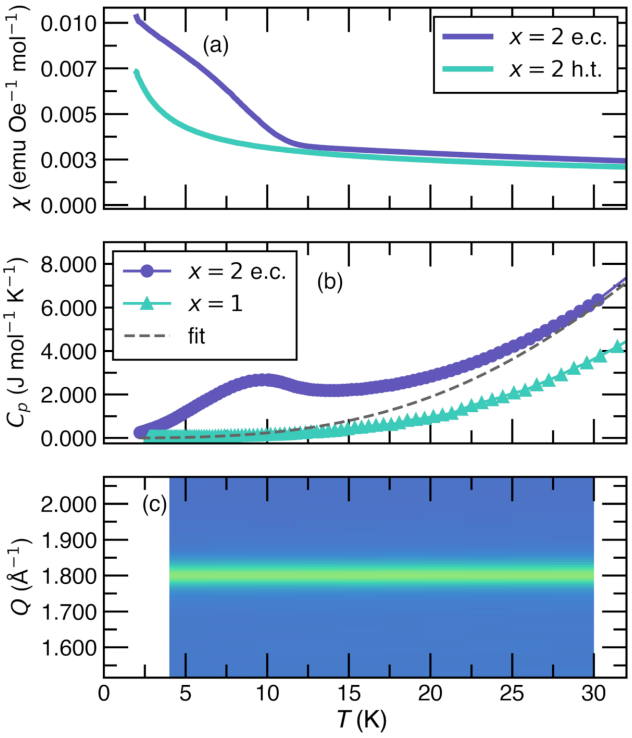

Figure 10: (a) Comparison of susceptibility measurements at $H = 0.1\,\mathrm{T}$ between the $Li_2ScMo_3O_8$ system prepared electrochemically (e.c.) and prepared through high-temperature solid state routes (h.t.). The h.t. sample is a reported quantum spin liquid and shows no long range magnetic order down to 2 K while the e.c. sample shows a feature, namely a prominent change in slope, at 12 K. (b) Heat capacity in zero applied field of the parent material $LiScMo_3O_8$ and $Li_2ScMo_3O_8$ (e.c.) shows a broad low temperature peak in the electrochemically lithiated sample. The dashed line is the fit of a model to a double-Debye function with two characteristic Debye temperatures. (c) Heat map of the integrated intensity of the $(31\bar{1})$ diffraction peak shows negligible changes in intensity in the temperature region of interest for the $Li_2ScMo_3O_8$ (e.c.) sample.

heat capacity was calculated by subtracting out the feature from the double-Debye fit. The integrated entropy as a function of temperature was found to be $S_m = 3.3\,\mathrm{J\,mol^{-1}\,K^{-1}}$ (figure displayed in the SI). For non-interacting spins that can be in one of two discrete states, the configurational entropy per mole would be $S_m = R\ln(2)$. This is an upper bound for the configurational entropy for discrete degrees of freedom. Even with a 20% error related to an undermeasurement of the sample mass, the integrated intensity would be $S_m = 4.3\,\mathrm{J\,mol^{-1}\,K^{-1}}$, still considerably lower than the upper bound. Although this experimental value of $S_m = 3.3\,\mathrm{J\,mol^{-1}\,K^{-1}}$ is lower compared to the expected value of $S_m = R\ln(2) = 5.76\,\mathrm{J\,mol^{-1}\,K^{-1}}$ for a spin 1/2 system, the relative order of magnitude of the experimental magnetic entropy is consistent with a bulk property of this system. There are a number of possible reasons for a lower value, including spin-orbit coupling effects. With one e^- distributed over three Mo atoms, any type of ordering in this system will be extremely subtle and difficult to fully establish. However, the heat capacity data qualitatively indicate a bulk transition, rather than possible impurity spins.

Despite the difficulty involved with the measurements and data interpretation, we turn to low-temperature neutron measurements in an effort to shed more light on a possible mechanism. There are no new magnetic peaks that appear below the feature temperature. A heat map of the integrated intensity of the $(31\bar{1})$ peak in Figure 10(c) shows negligible changes in intensity over the measured temperature range. The intensity changes for all peaks can be found in the SI. We find that the integrated intensity of the diffraction peaks remain constant where there are clear features found in susceptibility and heat capacity. We have established that nominally, the composition, structure, and density of states for both compounds are closely related. This raises the question of what is driving a low temperature feature in the electrochemically prepared material but not in the material prepared at high temperatures.

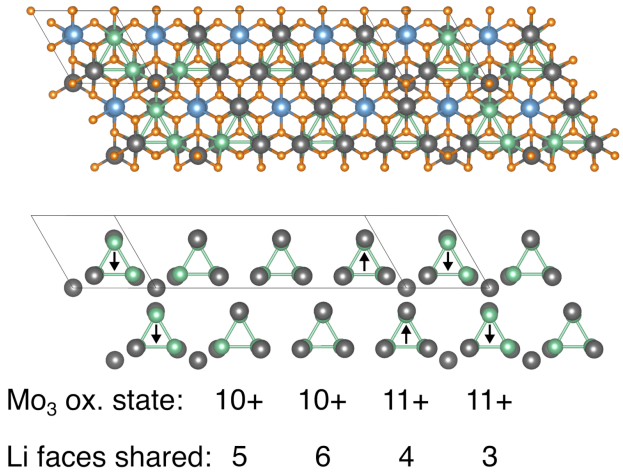

Figure 11: Full and simplified structure of a low-energy row ordering of Li at $x = 2.5$, annotated with the spin, formal oxidation state, and number of faces shared with Li octahedra (above and below) for each distinct Mo_3 cluster.

Coupling between charge, spin, and Li ordering

Previously we established a comprehensive picture of Li ordering in $Li_xScMo_3O_8$, in which the Li ions occupy only tetrahedral sites at $x = 1$, only octahedral sites at $x = 3$, and a mixture at intermediate x.[27] We also confirmed a preference for AFM coupling of the Mo_3 cluster moments at intermediate Li compositions ($1 < x < 3$), which in some cases even emerges when they are initialized ferromagnetically in DFT. At off-stoichiometric compositions, we expect electrons to remain localized and for there to be a mixture of oxidation states of the Mo_3 clusters. Indeed, analyzing the low-energy configurations considered previously reveals clear charge ordering, which can be inferred from both the average Mo-Mo bond length and total magnetic moment of each cluster.[27]

One such configuration at $x = 2.5$, shown in Figure 11, serves as an example of the coupling between charge, spin, and Li ordering in this system. The Li are arranged in a row ordering, with rows of tetrahedrally coordinated Li between regions of octahedrally coordinated Li. Of the four unique Mo_3 clusters, two have an oxidation state of 10+ and two have an oxidation state of 11+. The latter are arranged directly next to one another and carry magnetic spins which are antiparallel (along one direction of the supercell),

consistent with AFM coupling. Finally, counting the number of shared faces between Mo and Li octahedra reveals that the $[Mo_3]^{11+}$ clusters each share fewer Li faces than do the $[Mo_3]^{10+}$ clusters. This coupling serves to reduce the electrostatic energy penalty associated with face-sharing, as the clusters with higher oxidation state have fewer shared faces.

While this particular configuration is not expected to be a ground state of the true system, it illustrates the complex interplay between the different degrees of freedom. Even in the absence of long-range Li ordering, we expect that short-range Li ordering may couple to charge and spin ordering in a similar way. The role of Li ordering may explain differences in the magnetic behavior of the solid state and electrochemically prepared structures, since the two structures have different topologies of Li sites despite being composed of the same Mo_3 building blocks. In the $Li_2ScMo_3O_8$ (h.t.) structure, Li occupies only tetrahedral sites (which do not share faces with Mo octahedra) and each Mo has an identical environment. In the $Li_2ScMo_3O_8$ (e.c.) structure, due to the mixed tetrahedral/octahedral Li occupancy, some Mo share more faces with Li than others, spurring charge ordering at slightly off-stoichiometric x. Our results indicate that it is highly likely that this low temperature feature must be related to spin-spin correlations induced locally by Li ordering into $[Mo_3]^{11+}$ clusters. Electrochemical lithiation makes it difficult to deconvolute the effects of intrinsic Li ordering versus inhomogeneous lithiation, but regardless, Li ordering lowers the symmetry of the structure, lifts degeneracy, and can relieve magnetic frustration. The lifting of degeneracy due to Li ordering is reminiscent of spin-Jahn-Teller−ordering in geometrically frustrated magnetic oxide spinels.[52]

Conclusion

We demonstrate the utility of electrochemistry to precisely control the electron filling in a magnetic material. $LiScMo_3O_8$ has a Mo-based kagome network and serves as an effective platform for this study because this material is both a good lithium ion conductor

and is closely related to quantum spin liquid candidate $Li_2ScMo_3O_8$. Here, lithium was electrochemically inserted into the parent structure $Li_xScMo_3O_8$ from $x = 1.25$ to $x = 2.85$ by discharging a Swagelok cell versus Li metal. The resulting materials were characterized with magnetic measurements and showed that doped electrons remain localized on the Mo_3 clusters and agree with the proposed energy level diagram. DFT-based electronic structure calculations confirm localized partial charge densities and small dispersion for filled states. We find that metallicity cannot be induced through doping of a Mo kagome network and that it is unlikely to be realized in related systems. Low-temperature measurements indicate a spin correlation feature in electrochemically lithiated $Li_2ScMo_3O_8$ (e.c.) not present in high temperature $Li_2ScMo_3O_8$ (h.t.). This work indicates a likely coupling between charge, spin, and Li ordering due to electrochemical Li insertion. This study showcases how electrochemistry can serve as an avenue to tune the electronic structure in a frustrated magnetic material and provides additional understanding in the role of disorder in Mo-based kagome cluster magnets.

Supporting Information

The Supporting Information is available free of charge at [] with further details of the electrochemical Swagelok cell, diffraction, magnetic measurements, resistivity measurements, heat capacity measurements, and integrated intensity of neutron diffraction experiments.

Acknowledgments

This work was supported as part of the Center for Synthetic Control Across Length scales for Advancing Rechargeables (SCALAR), an Energy Frontier Research Center funded by the U.S. Department of Energy, Office of Science, Basic Energy Sciences under Award DE SC0019381. This research used computational resources of the National Energy Research

Scientific Computing Center (NERSC), a U.S. Department of Energy Office of Science User Facility located at Lawrence Berkeley National Laboratory, operated under Contract No. DE-AC02-05CH11231, and shared facilities of the UC Santa Barbara Materials Research Science and Engineering Center (MRSEC, NSF DMR 1720256), a member of the Materials Research Facilities Network (www.mrfn.org). We also acknowledge use of the shared computing facilities of the Center for Scientific Computing at UC Santa Barbara, supported by NSF CNS-1725797, and the NSF MRSEC at UC Santa Barbara, NSF DMR 1720256. We gratefully acknowledge support via the UC Santa Barbara NSF Quantum Foundry funded via the Q-AMASE-i program under award DMR-1906325. J.L.K. acknowledges support from the U.S. Department of Energy, Office of Science, Office of Advanced Scientific Computing Research, Department of Energy Computational Science Graduate Fellowship under Award Number DE-FG02-97ER25308. This research used resources of the Advanced Photon Source, a U.S. Department of Energy (DOE) Office of Science user facility operated for the DOE Office of Science by Argonne National Laboratory under Contract No. DE-AC02-06CH11357. A portion of this research used resources at the High Flux Isotope Reactor and the Spallation Neutron Source, a DOE Office of Science User Facility operated by the Oak Ridge National Laboratory.

References

(1) Johnston, W. D.; Heikes, R. R.; Sestrich, D. The Preparation, Crystallography, and Magnetic Properties of the $Li_xCo_{(1-x)}O$ System. *J. Phys. Chem. Solids* **1958**, *7*, 1–13.

(2) Mizushima, K.; Jones, P. C.; Wiseman, P. J.; Goodenough, J. B. Li_xCoO_2 ($0 < x < 1$): A New Cathode Material for Batteries of High Energy Density. *Mater. Res. Bull.* **1980**, *15*, 783–789.

(3) Nguyen, H.; Clément, R. J. Rechargeable Batteries from the Perspective of the Electron Spin. *ACS Energy Lett.* **2020**, *5*, 3848–3859.

(4) Motohashi, T.; Ono, T.; Sugimoto, Y.; Masubuchi, Y.; Kikkawa, S.; Kanno, R.; Karppinen, M.; Yamauchi, H. Electronic Phase Diagram of the Layered Cobalt Oxide System Li_xCoO_2 ($0.0 \leq x \geq 1.0$). *Phys. Rev. B* **2009**, *80*, 165114.

(5) Diethrich, T. J.; Gnewuch, S.; Dold, K. G.; Taddei, K. M.; Rodriguez, E. E. Tuning Magnetic Symmetry and Properties in the Olivine Series $Li_{1-x}Fe_xMn_{1-x}PO_4$ Through Selective Delithiation. *Chem. Mater.* **2022**, *34*, 5039–5053.

(6) Mukherjee, P.; Paddison, J. A. M.; Xu, C.; Ruff, Z.; Wildes, A. R.; Keen, D. A.; Smith, R. I.; Grey, C. P.; Dutton, S. E. Sample Dependence of Magnetism in the Next-Generation Cathode Material $LiNi_{0.8}Mn_{0.1}Co_{0.1}O_2$. *Inorg. Chem.* **2020**, *60*, 263–271.

(7) Griffith, K. J.; Seymour, I. D.; Hope, M. A.; Butala, M. M.; Lamontagne, L. K.; Preefer, M. B.; Koçer, C. P.; Henkelman, G.; Morris, A. J.; Cliffe, M. J.; Dutton, S. E.; Grey, C. P. Ionic and Electronic Conduction in $TiNb_2O_7$. *J. Am. Chem. Soc.* **2019**, *141*, 16706–16725.

(8) Preefer, M. B.; Saber, M.; Wei, Q.; Bashian, N. H.; Bocarsly, J. D.; Zhang, W.; Lee, G.; Milam-Guerrero, J.; Howard, E. S.; Vincent, R. C.; Melot, B. C.; Van der Ven, A.; Seshadri, R.; Dunn, B. S. Multielectron Redox and Insulator-to-Metal Transition upon

Lithium Insertion in the Fast-Charging, Wadsley-Roth Phase PNb_9O_{25}. *Chem. Mater.* **2020**, *32*, 4553–4563.

(9) Xia, Q.; Li, X.; Wang, K.; Li, Z.; Liu, H.; Wang, W., X.and Ye; Li, H.; Teng, X.; Pang, J.; Zhang, Q.; Ge, C.; Gu, L.; Miao, G.; Yan, S.; Hu, H.; Li, Q. Unraveling the Evolution of Transition Metals during Li Alloying–Dealloying by In-Operando Magnetometry. *Chem. Mater.* **2022**, *34*, 5852–5859.

(10) Romanenko, K.; Kuchel, P. W.; Jerschow, A. Accurate Visualization of Operating Commercial Batteries Using Specialized Magnetic Resonance Imaging with Magnetic Field Sensing. *Chem. Mater.* **2020**, *32*, 2107–2113.

(11) Wannier, G. H. Antiferromagnetism. The Triangular Ising Net. *Phys. Rev.* **1950**, *79*, 357.

(12) Ramirez, A. P. Strongly Geometrically Frustrated Magnets. *Annu. Rev. of Mater. Sci.* **1994**, *24*, 453–480.

(13) Balents, L. Spin Liquids in Frustrated Magnets. *Nature* **2010**, *464*, 199–208.

(14) Anderson, P. W. The Resonating Valence Bond State in La_2CuO_4 and Superconductivity. *Science* **1987**, *235*, 1196–1198.

(15) Norman, M. R. Colloquium: Herbertsmithite and the Search for the Quantum Spin Liquid. *Rev. Mod. Phys.* **2016**, *88*, 041002.

(16) Shores, M. P.; Nytko, E. A.; Bartlett, B. M.; Nocera, D. G. A Structurally Perfect S= 1/2 Kagome Antiferromagnet. *J. Am. Chem. Soc.* **2005**, *127*, 13462–13463.

(17) Sheckelton, J. P.; Neilson, J. R.; Soltan, D. G.; McQueen, T. M. Possible Valence-Bond Condensation in the Frustrated Cluster Magnet $LiZn_2Mo_3O_8$. *Nat. Mater.* **2012**, *11*, 493–496.

(18) Jiao, L.; Xu, Q.; Cheon, Y.; Sun, Y.; Felser, C.; Liu, E.; Wirth, S. Signatures for Half-Metallicity and Nontrivial Surface States in the Kagome Lattice Weyl Semimetal $Co_3Sn_2S_2$. *Phys. Rev. B* **2019**, *99*, 245158.

(19) Ortiz, B. R.; Gomes, L. C.; Morey, J. R.; Winiarski, M.; Bordelon, M.; Mangum, J. S.; Oswald, I. W. H.; Rodriguez-Rivera, J. A.; Neilson, J. R.; Wilson, S. D.; Ertekin, E.; McQueen, T. M.; Toberer, E. S. New Kagome Prototype Materials: Discovery of KV_3Sb_5, RbV_3Sb_5, and CsV_3Sb_5. *Phys. Rev. Mat.* **2019**, *3*, 094407.

(20) Chen, Q.; Sinclair, R.; Akbari-Sharbaf, A.; Huang, Q.; Dun, Z.; Choi, E. S.; Mourigal, M.; Verrier, A.; Rouane, R.; Bazier-Matte, X.; Quilliam, J. A.; Aczel, A. A.; Zhou, H. D. Magnetic Order and Spin Liquid Behavior in $[Mo_3]^{11+}$ Molecular Magnets. *Phys. Rev. Mater.* **2022**, *6*, 044414.

(21) Iida, K.; Yoshida, H.; Okabe, H.; Katayama, N.; Ishii, Y.; Koda, A.; Inamura, Y.; Murai, N.; Ishikado, M.; Kadono, R.; Kajimoto, R. Quantum magnetisms in uniform triangular lattices $Li_2AMo_3O_8$ (A= In, Sc). *Sci. Rep.* **2019**, *9*, 1–9.

(22) Sheckelton, J. P.; Foronda, F. R.; Pan, L.; Moir, C.; McDonald, R. D.; Lancaster, T.; Baker, P. J.; Armitage, N. P.; Imai, T.; Blundell, S. J.; McQueen, T. M. Local Magnetism and Spin Correlations in the Geometrically Frustrated Cluster Magnet $LiZn_2Mo_3O_8$. *Phys. Rev. B* **2014**, *89*, 064407.

(23) Mourigal, M.; Fuhrman, W. T.; Sheckelton, J. P.; Wartelle, A.; Rodriguez-Rivera, J. A.; Abernathy, D. L.; McQueen, T. M.; Broholm, C. L. Molecular Quantum Magnetism in $LiZn_2Mo_3O_8$. *Phys. Rev. Lett.* **2014**, *112*, 027202.

(24) Khomskii, D. I.; Streltsov, S. V. Orbital Effects in Solids: Basics, Recent Progress, and Opportunities. *Chem. Rev.* **2020**, *121*, 2992–3030.

(25) Nikolaev, S. A.; Solovyev, I. V.; Streltsov, S. V. Quantum Spin Liquid and Cluster Mott Insulator Phases in the Mo_3O_8 Magnets. npj *Quantum Mater.* **2021**, *6*, 1–8.

(26) Chen, G.; Kee, H.; Kim, Y. B. Cluster Mott Insulators and Two Curie-Weiss Regimes on an Anisotropic Kagome Lattice. *Phys. Rev. B* **2016**, *93*, 245134.

(27) Wyckoff, K. E.; Kaufman, J. L.; Baek, S. W.; Dolle, C.; Zak, J. J.; Bienz, J.; Kautzsch, L.; Vincent, R. C.; Zohar, A.; See, K. A.; Eggeler, Y. M.; Pilon, L.; Van der Ven, A.; Seshadri, R. Metal–Metal Bonding as an Electrode Design Principle in the Low-Strain Cluster Compound $LiScMo_3O_8$. *J. Am. Chem. Soc.* **2022**, *144*, 5841–5854.

(28) Haraguchi, Y.; Michioka, C.; Imai, M.; Ueda, H.; Yoshimura, K. Spin-Liquid Behavior in the Spin-Frustrated Mo_3 Cluster Magnet $Li_2ScMo_3O_8$ in Contrast to Magnetic Ordering in Isomorphic $Li_2InMo_3O_8$. *Phys. Rev. B* **2015**, *92*, 014409.

(29) Akbari-Sharbaf, A.; Sinclair, R.; Verrier, A.; Ziat, D.; Zhou, H. D.; Sun, X. F.; Quilliam, J. A. Tunable Quantum Spin Liquidity in the 1/6 th-Filled Breathing Kagome Lattice. *Phys. Rev. Lett.* **2018**, *120*, 227201.

(30) Radin, M. D.; Van der Ven, A. Stability of Prismatic and Octahedral Coordination in Layered Oxides and Sulfides Intercalated with Alkali and Alkaline-Earth mMetals. *Chem. Mater* **2016**, *28*, 7898–7904.

(31) Cheetham, A. K.; Seshadri, R.; Wudl, F. Chemical Synthesis and Materials Discovery. *Nature Synthesis* **2022**, 1–7.

(32) Calder, S.; An, K.; Boehler, R.; Dela Cruz, C. R.; Frontzek, M. D.; Guthrie, M.; Haberl, B.; Huq, A.; Kimber, S. A. J.; Liu, J.; Molaison, J. J.; Neuefeind, J.; Page, K.; dos Santos, A. M.; Taddei, K. M.; Tulk, C.; Tuker, M. G. A Suite-Level Review of the Neutron Powder Diffraction Instruments at Oak Ridge National Laboratory. *Rev. Sci. Instrum.* **2018**, *89*, 092701.

(33) Neuefeind, J.; Feygenson, M.; Carruth, J.; Hoffmann, R.; Chipley, K. K. The Nanoscale Ordered Materials Diffractometer NOMAD at the Spallation Neutron Source SNS. *Nucl. Instrum. Methods Phys. Res. B* **2012**, *287*, 68–75.

(34) DeBenedittis, J.; Katz, L. Complex Metal Oxides of the Type $AMMo_3^{IV}O_8$. *Inorg. Chem.* **1965**, *4*, 1836–1839.

(35) Coelho, A. A. *TOPAS* and *TOPAS-Academic*: An Optimization Program Integrating Computer Algebra and Crystallographic Objects Written in C++. *J. Appl. Crystallogr.* **2018**, *51*, 210–218.

(36) Liu, J.; Du, Z.; Wang, X.; Tan, S.; Wu, X.; Geng, L.; Song, B.; Chien, P.; Michelle Everett, S.; Hu, E. Anionic Redox Induced Anomalous Structural Transition in Ni-rich Cathodes. *Energy Environ. Sci.* **2021**, *14*, 6441–6454.

(37) Zhang, Y.; Liu, J.; Tucker, M. G. Lorentz Factor for Time-of-Flight Neutron Bragg and Total Scattering. *Acta Crystallogr. A* **2023**, *79*.

(38) Borkiewicz, O. J.; Shyam, B.; Wiaderek, K. M.; Kurtz, C.; Chupas, P. J.; Chapman, K. W. The AMPIX Electrochemical Cell: A Versatile Apparatus for In Situ X-ray Scattering and Spectroscopic Measurements. *J. Appl. Crystallogr.* **2012**, *45*, 1261–1269.

(39) Momma, K.; Izumi, F. *VESTA 3* For Three-Dimensional Visualization of Crystal, Volumetric and Morphology Data. *J. Appl. Crystallogr.* **2011**, *44*, 1272–1276.

(40) Kresse, G.; Hafner, J. Ab Initio Molecular Dynamics for Liquid Metals. *Phys. Rev. B* **1993**, *47*, 558–561.

(41) Kresse, G.; Hafner, J. Ab Initio Molecular-Dynamics Simulation of the Liquid-Metal–Amorphous-Semiconductor Transition in Germanium. *Phys. Rev. B* **1994**, *49*, 14251–14269.

(42) Kresse, G.; Furthmüller, J. Efficiency of Ab-Initio Total Energy Calculations for Metals and Semiconductors Using a Plane-Wave Basis Set. *Computational Mater. Sci.* **1996**, *6*, 15–50.

(43) Kresse, G.; Furthmüller, J. Efficient Iterative Schemes for Ab Initio Total-Energy Calculations Using a Plane-Wave Basis Set. *Phys. Rev. B* **1996**, *54*, 11169–11186.

(44) Blöchl, P. E. Projector Augmented-Wave Method. *Phys. Rev. B* **1994**, *50*, 17953–17979.

(45) Kresse, G.; Joubert, D. From Ultrasoft Pseudopotentials to the Projector Augmented-Wave Method. *Phys. Rev. B* **1999**, *59*, 1758–1775.

(46) Monkhorst, H. J.; Pack, J. D. Special Points for Brillouin-Zone Integrations. *Phys. Rev. B* **1976**, *13*, 5188–5192.

(47) Blöchl, P. E.; Jepsen, O.; Andersen, O. K. Improved Tetrahedron Method for Brillouin-Zone Integrations. *Phys. Rev. B* **1994**, *49*, 16223–16233.

(48) Sun, J.; Ruzsinszky, A.; Perdew, J. P. Strongly Constrained and Appropriately Normed Semilocal Density Functional. *Phys. Rev. Lett.* **2015**, *115*, 036402.

(49) Sun, J.; Remsing, R. C.; Zhang, Y.; Sun, Z.; Ruzsinszky, A.; Peng, H.; Yang, Z.; Paul, A.; Waghmare, U.; Wu, X.; Klein, M. L.; Perdew, J. P. Accurate First-Principles Structures and Energies of Diversely Bonded Systems from an Efficient Density Functional. *Nat. Chem.* **2016**, *8*, 831–836.

(50) Haraguchi, Y.; Michioka, C.; Ueda, H.; Yoshimura, K. Charge Fluctuation in $S = 1/2$ Triangular Lattice Cluster Antiferromagnets $Li_2ScMo_3O_8$ and $Li_2InMo_3O_8$. *J. Phys.: Conf. Series* **2017**, *868*, 012022.

(51) Fortes, A. D.; Wood, I. G.; Brodholt, J. P.; Alfredsson, M.; Vočadlo, L.; McGrady, G. S.; Knight, K. S. A High-Resolution Neutron Powder Diffraction Study of Ammonia Dihydrate ($ND_3{\cdot}2D_2O$) phase I. *Chem. Phys.* **2003**, *119*, 10806–10813.

(52) Kemei, M. C.; Barton, P. T.; Moffitt, S. L.; Gaultois, M. W.; Kurzman, J. A.; Seshadri, R.; Suchomel, M. R.; Kim, Y. Crystal Structures of Spin-Jahn–Teller-Ordered $MgCr_2O_4$ and $ZnCr_2O_4$. *J. Phys. Condens. Matter* **2013**, *25*, 326001.

Graphical TOC Entry

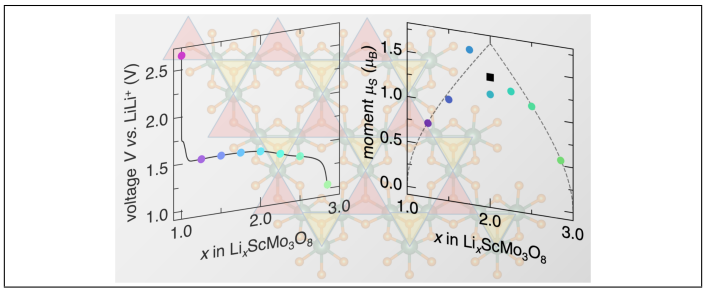

Supporting Information:

Electrochemical Control of Magnetism on the Breathing Kagome Network of $Li_xScMo_3O_8$

Kira E. Wyckoff,[†] Linus Kautzsch,[†] Jonas L. Kaufman,[†] Brenden R. Ortiz,[‡] Anna Kallistova,[†] Ganesh Pokharel,[‡] Jue Liu,[¶] Keith M. Taddei,[¶] Kamila M. Wiaderek,[§] Saul H. Lapidus,[‖] Stephen D. Wilson,[⊥] Anton Van der Ven,[*,†] and Ram Seshadri[*,†]

†*Materials Department and Materials Research Laboratory*
University of California, Santa Barbara, California 93106, United States
‡*Materials Department and California Nanosystems Institute*
University of California, Santa Barbara, California 93106, United States
¶*Neutron Scattering Division, Oak Ridge National Laboratory*
Oak Ridge, Tennessee, 37831, United States
§*X-ray Science Division, Advanced Photon Source, Argonne National Laboratory, Lemont, Illinois, 60439, United States*
‖*Joint Center for Energy Storage Research and X-ray Science Division, Advanced Photon Source, Argonne National Laboratory, Lemont, Illinois, 60439, United States*
⊥*Materials Department*
University of California, Santa Barbara, California 93106, United States
#*Department of Chemistry and Biochemistry*
University of California, Santa Barbara, California 93106, United States

E-mail: avdv@ucsb.edu; seshadri@mrl.ucsb.edu

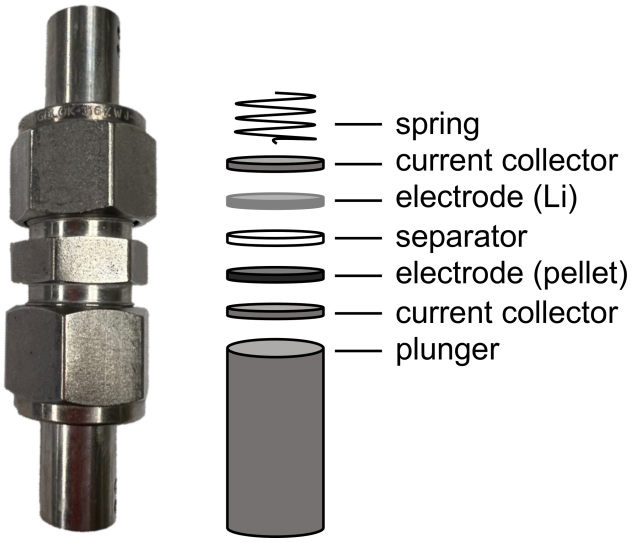

Figure 1: Diagram showing a picture of an experimental swagelok cell on the right and a corresponding schematic of the internal components on the left. For electrochemical lithiation, one electrode of the cell is Li metal and the other electrode is a pressed pellet of $LiScMo_3O_8$. The electrodes are separated with a glass fiber separator saturated in electrolyte and the entire stack is kept under light pressure with a metal spring The current collectors are made of stainless steel.

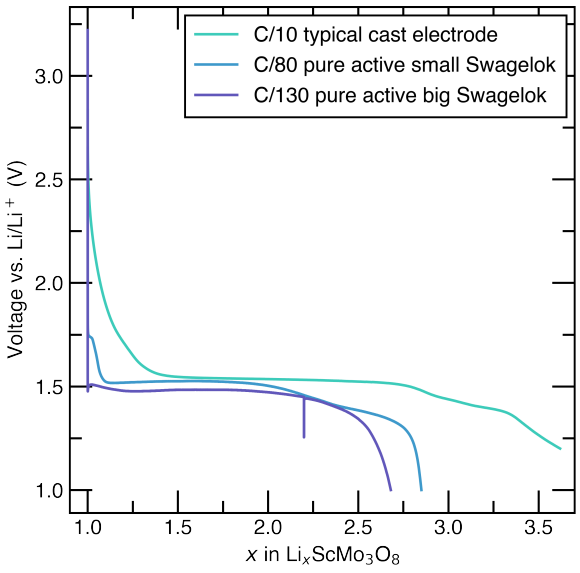

Figure 2: Overlay of electrochemical discharge curves comparing pressed pellets of pure active material cycled in both small and large Swagelok cells, compared to a typical composite cast electrode. There is slight overpotential introduced by omitting binder and conductive carbon. Additionally, the structure of the discharge curves smooth with increasing sample size.

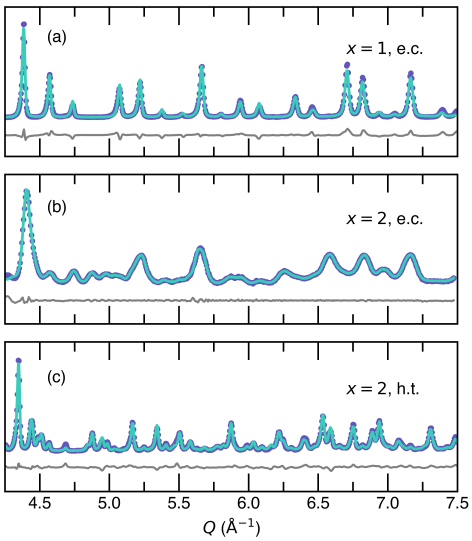

Figure 3: Neutron powder Bragg diffraction data and refinements for (a) $LiScMo_3O_8$ (Rietveld refinement on NOMAD data to $P3m1$ space group), (b) $Li_2ScMo_3O_8$ (e.c.) (Pawley refinement on WAND^2 data to $C2$ space group), and (c) $Li_2ScMo_3O_8$ (h.t.) (Rietveld refinement on NOMAD data to $P6_3mc$ space group) shows single phases for all materials. Refinement statistics can be found in the following tables.

The starting material $LiScMo_3O_8$ was characterized with neutron powder diffraction at the NOMAD beamline located at Oak Ridge National Laboratory. Rietveld refinement of $LiScMo_3O_8$ in Figure 3(a) shows good agreement with the expected structure. Electrochemically prepared $Li_2ScMo_3O_8$ (e.c.) was characterized with neutron powder diffraction at the WAND^2 HB-2C beamline at Oak Ridge National Laboratory and shows a single phase from a Pawley refinement to an indexed space group that is closely related to the parent structure. Previous experiments show that the $Li_2ScMo_3O_8$ (e.c.) material stays highly crystalline and the broad peaks shown here are due to the momentum resolution on the WAND^2 HB-2C beamline. High-temperature $Li_2ScMo_3O_8$ (h.t.) was also characterized with neutron powder diffraction at the NOMAD beamline and shows good agreement with the accepted structure. Atomic positions can be found in the included CIF files for these refinements.

Table 1: Summary of refinement parameters from Figure 3 (a) in the Supporting Information from a Rietveld refinement on NOMAD data bank 5 for $LiScMo_3O_8$.

$LiScMo_3O_8$	
parameter	value
lattice constant	a = 5.72358(9) Å c = 4.94235(9) Å
space group	$P3m1$
R_{wp}	8.75
R_{exp}	0.72
GOF = R_{wp}/R_{exp}	12.15

Table 2: Summary of refinement parameters from Figure 3 (b) in the Supporting Information from a Pawley refinement on WAND^2 data for $Li_2ScMo_3O_8$ (e.c.).

$Li_2ScMo_3O_8$ (e.c.)	
parameter	value
lattice constant	a = 10.37199(8) Å b = 9.90785(8) Å c = 3.04370(8) Å
space group	$C2$
R_{wp}	1.81
R_{exp}	20.01
GOF = R_{wp}/R_{exp}	0.09

Table 3: Summary of refinement parameters from Figure 3 (c) in the Supporting Information from a Rietveld refinement on NOMAD data bank 5 for $Li_2ScMo_3O_8$ (h.t.).

$Li_2ScMo_3O_8$ (h.t.)

parameter	value
lattice constant	a = 5.77107(7) Å c = 10.29286(3) Å
space group	$P6_3mc$
R_{wp}	9.51
R_{exp}	0.60
GOF = R_{wp}/R_{exp}	15.85

Table 4: Summary of refinement parameters from Figure 5 (a) in the main text from a Rietveld refinement on $Li_2ScMo_3O_8$ (e.c.). The R_{wp} is 12.53, the R_{exp} is 8.86, and the GOF is 2.14. The space group is *P1*.

a	5.7224(5)
b	7.5748(8)
c	7.576(1)
α	81.733(8)°
β	67.77(1)°
γ	67.795(7)°

site	x	y	z	occ
Li1	0.998973	0.181235	0.819429	1
Li2	0.833318	0.819686	0.514381	1
Li3	0.319834	0.570296	0.266863	1
Li4	0.842511	0.571096	0.266899	1
Mo1	0.82(1)	0.30(1)	0.51(1)	1
Mo2	0.82(1)	0.81(1)	0.00(1)	1
Mo3	0.37(1)	0.31(1)	0.50(1)	1
Mo4	0.82(1)	0.58(1)	0.80(1)	1
Mo5	0.82(1)	0.09(1)	0.28(1)	1
Mo6	0.37(1)	0.82(1)	0.01(1)	1
O1	0.161375	0.368118	0.792542	1
O2	0.160129	0.128359	0.551021	1
O3	0.159852	0.866374	0.295562	1
O4	0.661441	0.599414	0.077696	1
O5	0.670963	0.090764	0.567302	1
O6	0.502138	0.027209	0.968808	1
O7	0.503866	0.528719	0.463267	1
O8	0.995221	0.287411	0.221486	1
O9	0.995775	0.777433	0.716441	1
O10	0.677749	0.368280	0.792407	1
O11	0.678310	0.866258	0.295568	1
O12	0.161290	0.623571	0.053998	1
O13	0.510649	0.777398	0.716385	1
O14	0.495931	0.287302	0.221520	1
O15	0.001795	0.000515	0.996074	1
O16	0.000104	0.507315	0.492484	1
Sc1	0.32(1)	0.83(2)	0.53(1)	1
Sc2	0.34(1)	0.33(2)	0.97(1)	1

Table 5: Summary of refinement parameters from Figure 5 (b) in the main text from a Rietveld refinement on $Li_3ScMo_3O_8$ (e.c.). The R_{wp} is 8.70, the R_{exp} is 5.98, and the GOF is 1.45. The space group is *P1*.

a	5.1514(1)
b	5.70220(6)
c	5.70220(6)
α	120°
β	90°
γ	90°

site	x	y	z	occ
Li1	0.305400	0.159078	0.318156	1
Li2	0.305400	0.681844	0.840922	1
Li3	0.305400	0.159078	0.840922	1
Mo1	0.837(1)	0.156(1)	0.335(1)	1
Mo2	0.837(1)	0.591(2)	0.793(1)	1
Mo3	0.837(1)	0.155(1)	0.792(1)	1
O1	0.565219	0.840652	0.681304	1
O2	0.565219	0.318696	0.159348	1
O3	0.080746	0.012449	0.506225	1
O4	0.080746	0.493775	0.987551	1
O5	0.525212	0.333333	0.666667	1
O6	0.565219	0.840652	0.159348	1
O7	0.080746	0.493775	0.506225	1
O8	0.016381	0.000000	0.000000	1
Sc1	0.257(3)	0.666667	0.333333	1

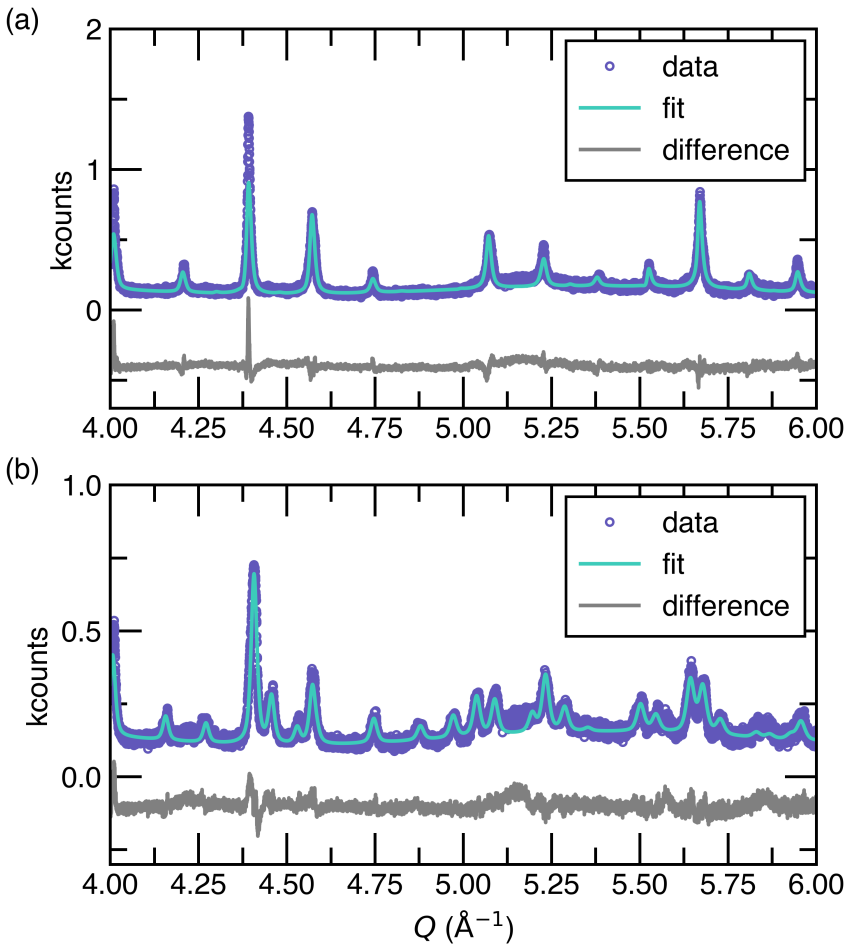

Figure 4: Rietveld refinements of (a) $Li_2ScMo_3O_8$ (e.c.) and (b) $Li_3ScMo_3O_8$ (e.c.) of *operando* synchrotron powder diffraction data collected at 11-BM at APS. These diffraction patterns were extracted from the *operando* AMPIX experiment and fit to the calculated ground state structures. The backgrounds were fit and only the lattice parameters and transition metal sites were allowed to refine. This figure shows the high Q region only.

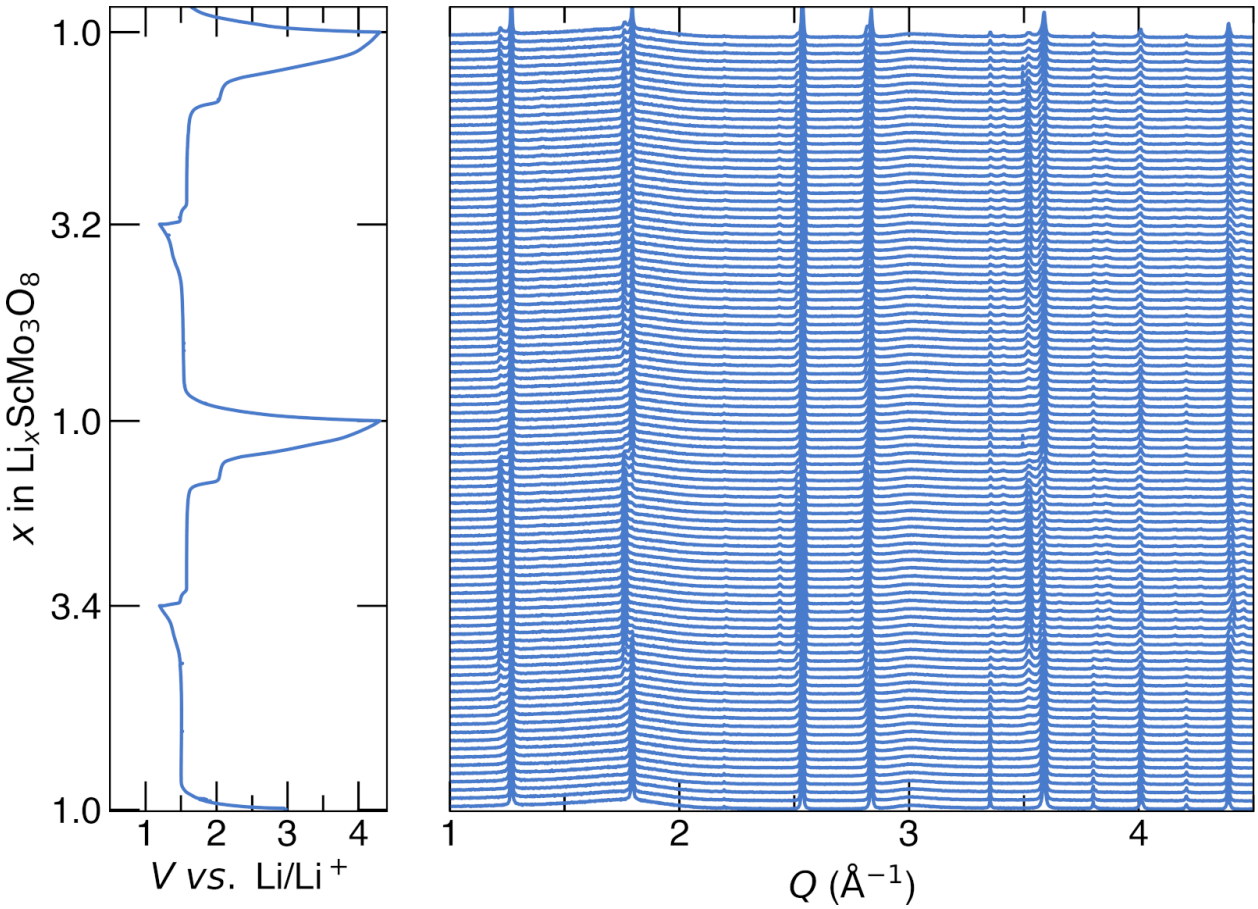

Figure 5: *Operando* synchrotron X-ray diffraction of $LiScMo_3O_8$ during the first two galvanostatic discharge/charge cycles at a C/15 cycling rate. The electrochemistry is shown in the left panel.

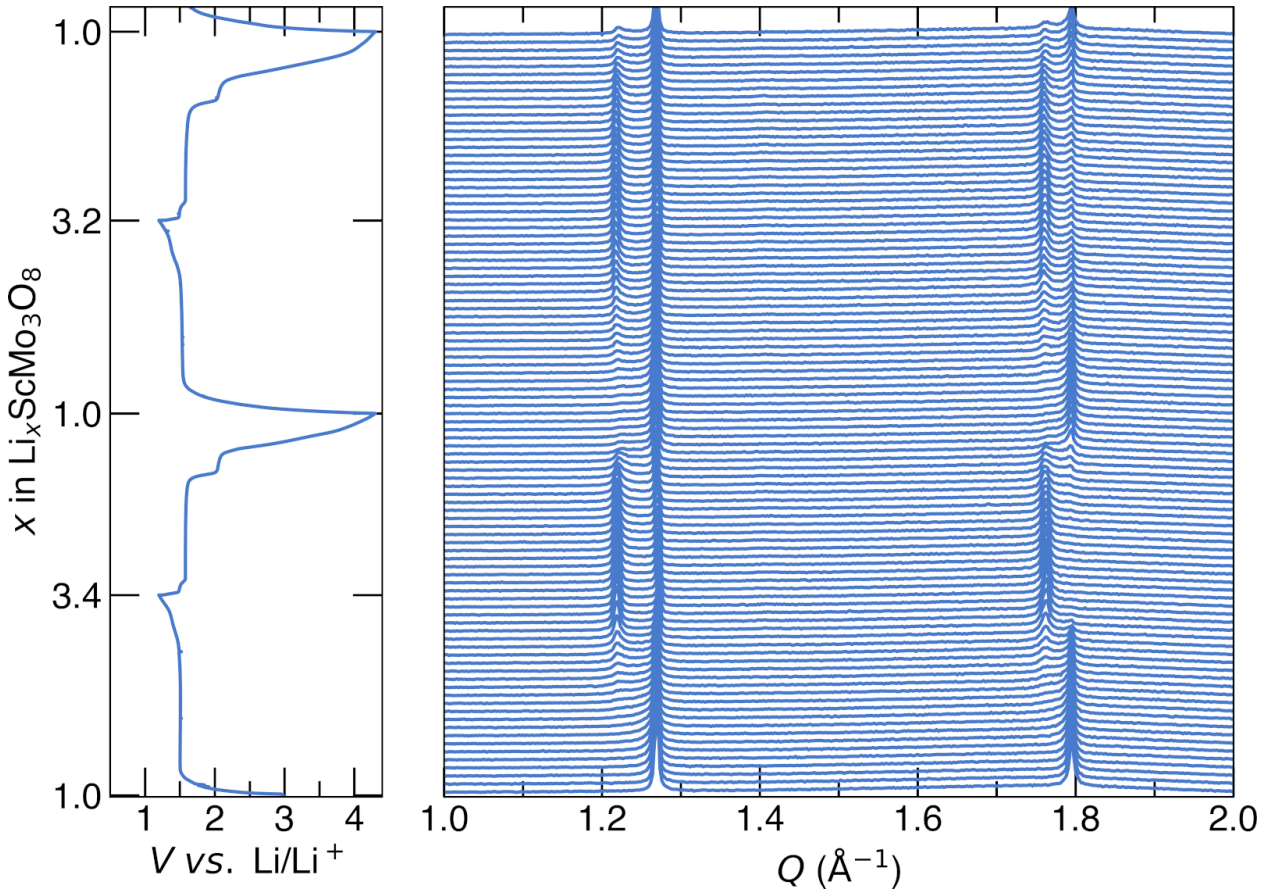

Figure 6: *Operando* synchrotron X-ray diffraction of $LiScMo_3O_8$ during the first two galvanostatic discharge/charge cycles at a C/15 cycling rate. The electrochemistry is shown in the left panel. The right panel shows the diffraction data at low Q.

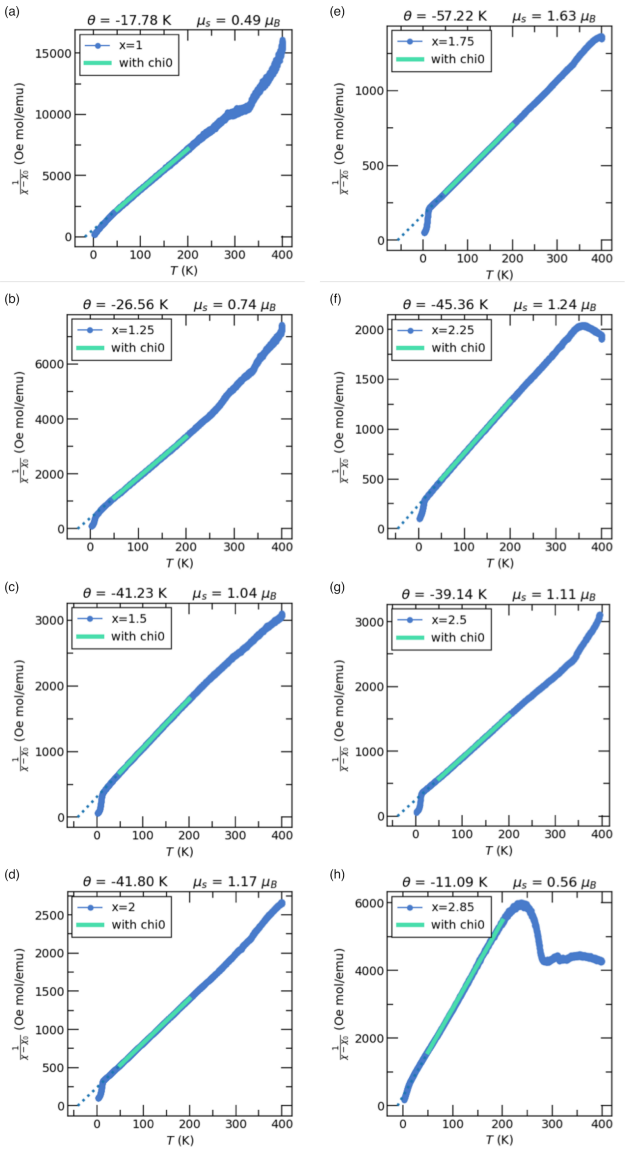

Figure 7: Curie-Weiss fits for all of the electrochemically prepared samples from 50 K to 200 K.

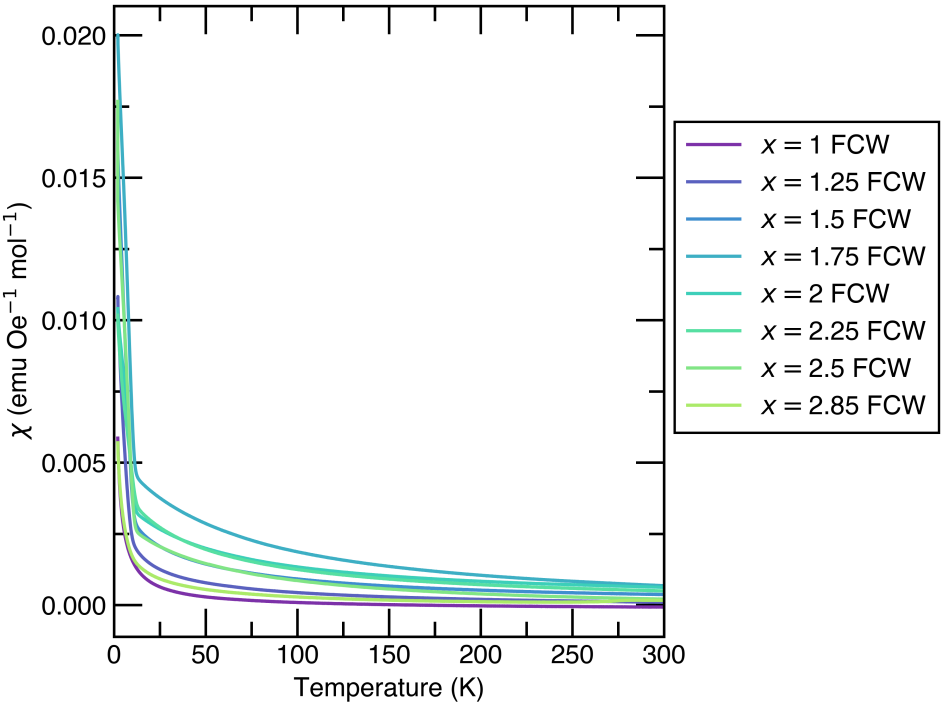

Figure 8: Overlay of the field-cooled warming susceptibility data as a function of temperature for all of the samples.

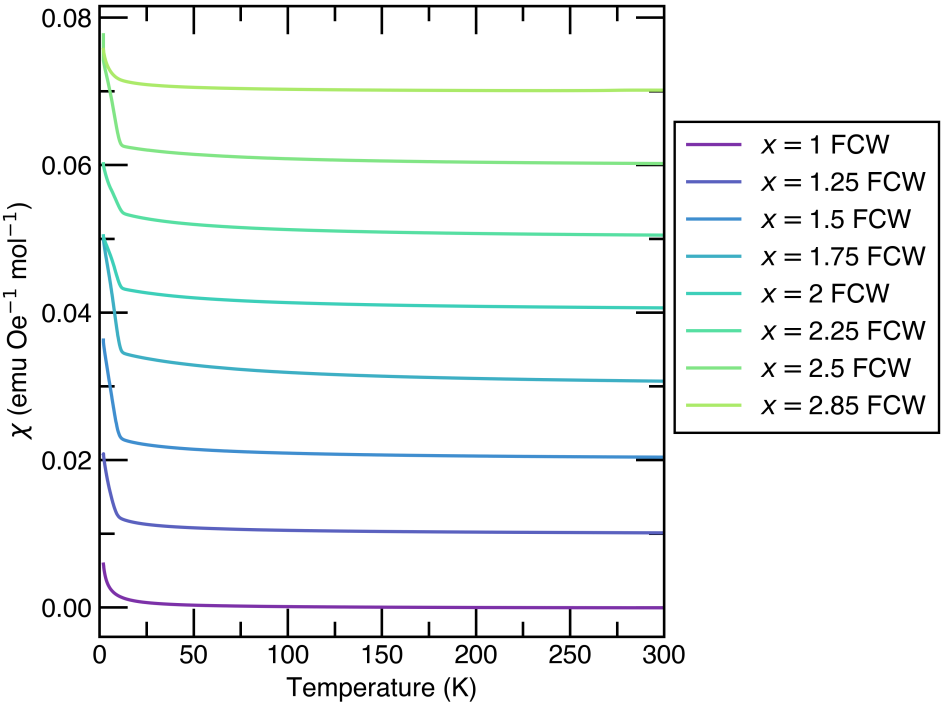

Figure 9: Offset of the field-cooled warming susceptibility data as a function of temperature for all of the samples.

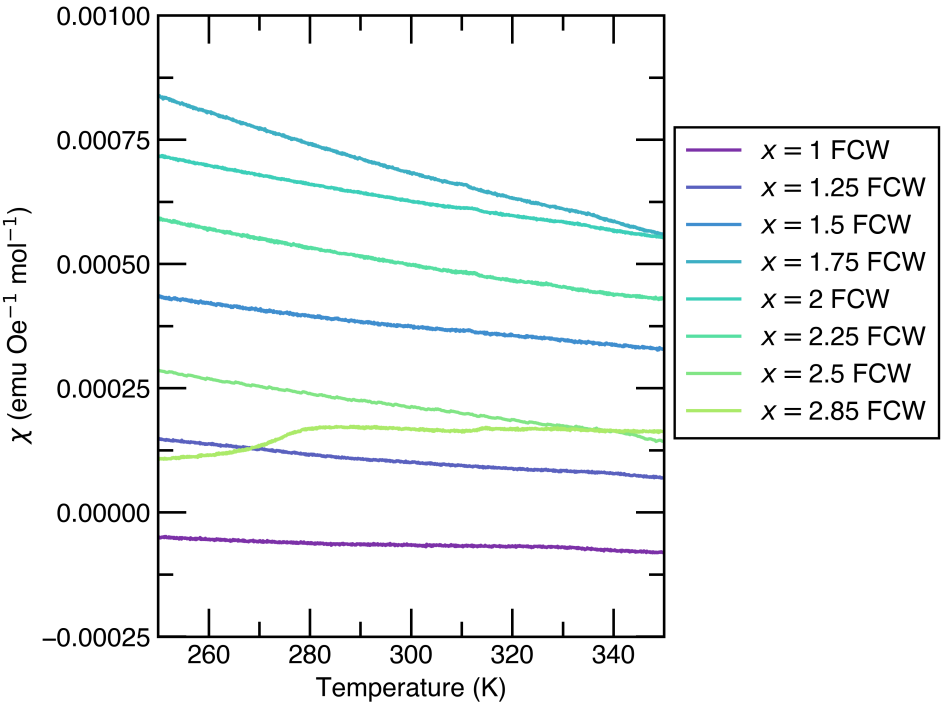

Figure 10: Overlay and zoom of the high-temperature regime of the field-cooled warming susceptibility data as a function of temperature for all of the samples.

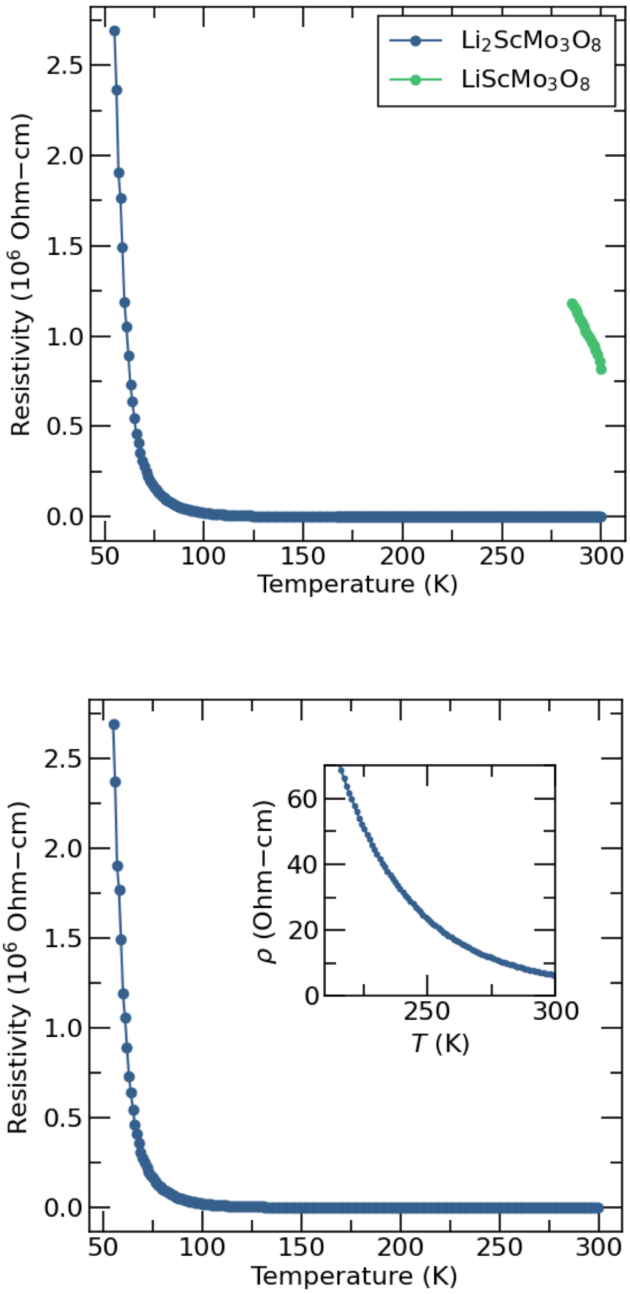

Figure 11: (top) Resistivity data for $Li_2ScMo_3O_8$ (h.t.) and $LiScMo_3O_8$ taken using a 4-point probe measurement on a Quantum Design PPMS. $Li_2ScMo_3O_8$ (h.t.) displays nearly 6 orders of magnitude lower resistivty than $LiScMo_3O_8$. (bottom) Resistivity data for $Li_2ScMo_3O_8$ (h.t.) with an inset highlighting the significantly lower resistivity value close to room temperature.

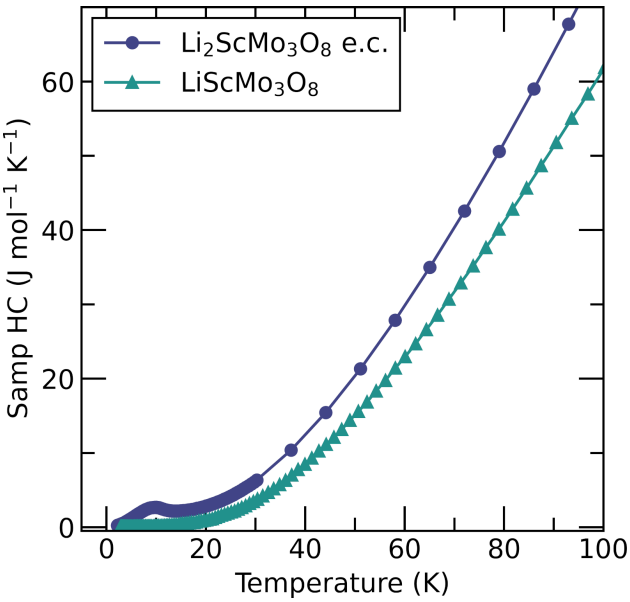

Figure 12: Heat capacity for $Li_2ScMo_3O_8$ (e.c.) and $LiScMo_3O_8$ from 3 K to 100 K.

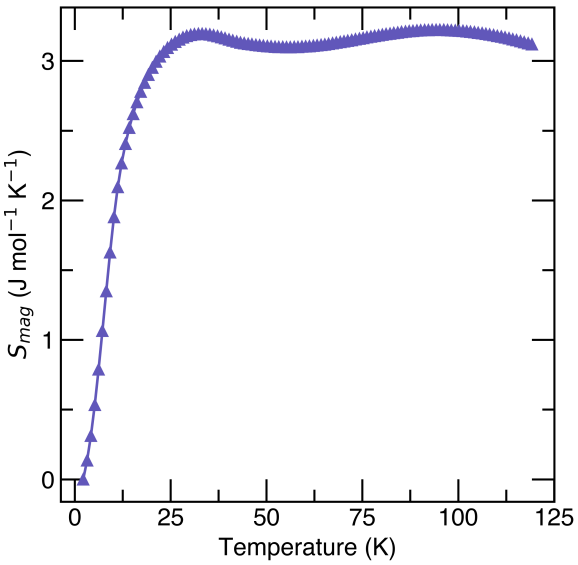

Figure 13: Magnetic entropy as a function of temperature for $Li_2ScMo_3O_8$ (e.c.).

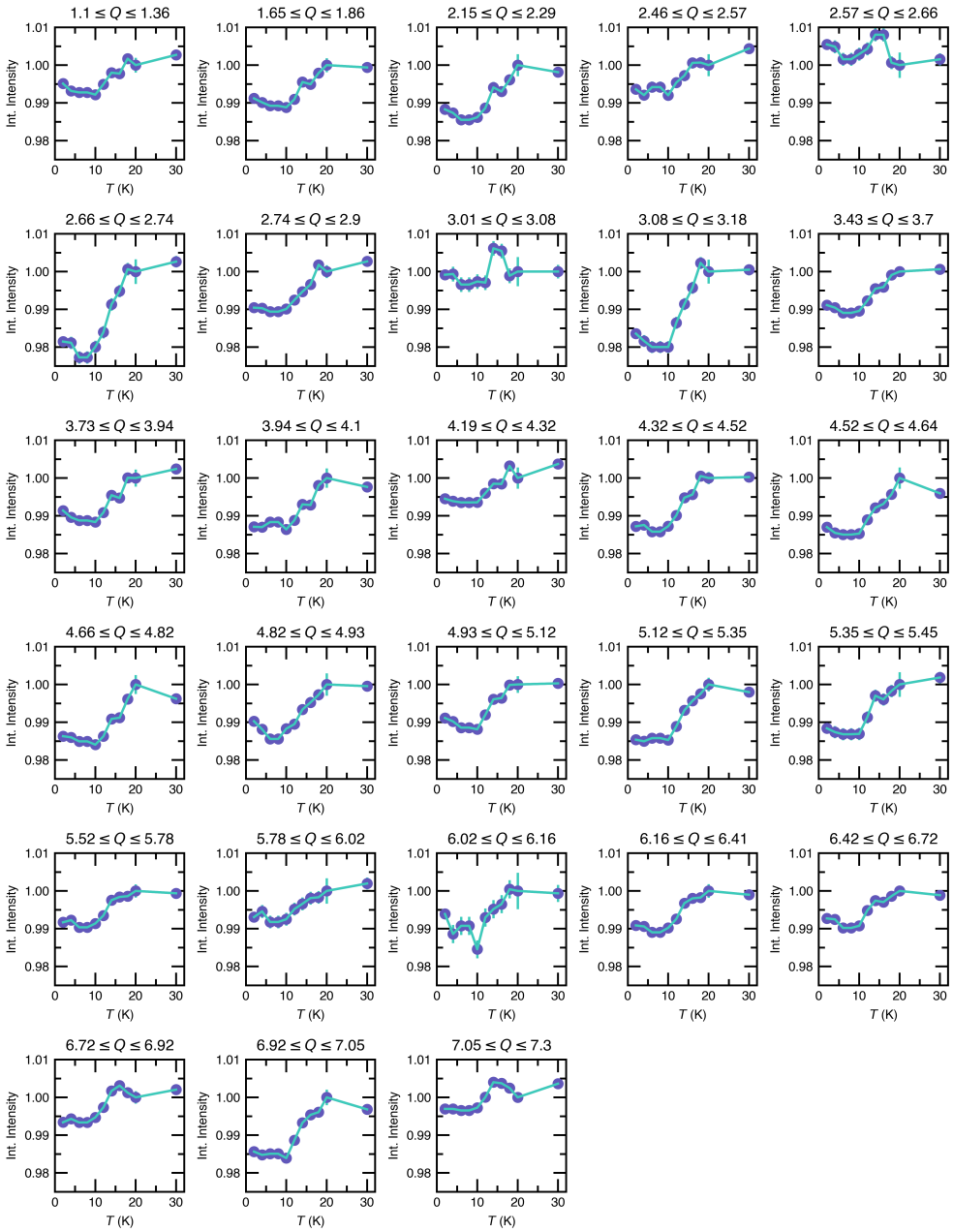

Figure 14: Integrated intensity for every diffraction peak as a function of temperature for $Li_2ScMo_3O_8$ (e.c.) from neutron diffraction data taken on WAND^2 beamline at Oak Ridge National Laboratory.